In vitro antibacterial properties of $MoO_3/SiO_2/Ag_2O$ nanocomposite coating prepared by double cathode glow discharge technique

Yanjie Zhao[a], Jiang Xu[a,*], Zhengyang Li[b], Tao Fu[c], Shuyun Jiang[d]

[a] Department of Material Science and Engineering, Nanjing University of Aeronautics and Astronautics, 29 Yudao Street, Nanjing 210016, PR China
[b] Institute of Mechanics, Chinese Academy of Sciences, Beijing 100190, PR China
[c] School of Life Science and Technology, Xi'an Jiaotong University, Xi'an 710049, PR China
[d] Department of Mechanical Engineering, Southeast University, 2 Si Pai Lou, Nanjing 210096, PR China

ABSTRACT

To obtain a self-disinfecting surface to combat nosocomial infections, in situ synthesis of the MoO_3-SiO_2-Ag_2O nanocomposite antibacterial coating was prepared onto Ti–6Al–4V substrate via a double cathode glow discharge technique conducted in a Ar + O_2 gas mixture. The phase composition, microstructure and chemical structure of the as-prepared coating were systematically characterized by means of a series of microscopic examination methods. The microstructure of the coating exhibited an amorphous/nanocrystalline architecture, and both the MoO_3 and Ag_2O crystallites were evenly embedded in an amorphous SiO_2 matrix. Photocatalytic activities of the coating were evaluated by photodegradation of rhodamine B (RhB) dye. The results showed that the introduction of Ag_2O enhanced photocatalytic activity of the MoO_3-SiO_2 nanocomposite coating. In vitro antibacterial activity of the MoO_3-SiO_2-Ag_2O coating against Gram-negative bacteria, Gram-positive bacteria and fungi were investigated and compared with that of the MoO_3-SiO_2 coating under both dark and visible light conditions. The MoO_3-SiO_2-Ag_2O coating possessed higher bactericidal activities than the MoO_3-SiO_2 coating, due to the combined effects of surface hydrophobicity, the release of Ag^+ ions, surface acidic reaction and photocatalytic activity.

1. Introduction

Nowadays, bacterial diseases, referred to any of a variety of diseases caused by bacteria infections, pose a constant and grave threat to human health worldwide. It is reported by World Health Organization that approximately 1.4 million people suffer from serious infections by human pathogen in healthcare environments (nosocomial infections), which are considered as the fourth leading cause of disease in developed countries [1]. Such infections are inextricably bound to the transmission of the presence of nosocomial pathogenic microbes from contaminated surfaces of installations and medical devices to healthy persons or patients [2]. Under a microbially contaminated hospital environment, the spread of infectious pathogens is difficult to control effectively through hand hygiene or medical device sterilization [3]. In addition, some formidable nosocomial pathogens, such as methicillin-resistant *Staphylococcus aureus* (MRSA) [4] and vancomycin-resistant Enterococci (VRE) [5], have already shown much more resistant against currently available antibiotics used in modern medicine, aggravating the severity of nosocomial infections [6].

Most metallic medical devices lack any antibacterial activity to impede the attachment and colonization of pathogenic bacteria on their surfaces. For instance, Ti and Ti-based alloys [7], widely utilized as surgical implanted biomaterials, are frequently susceptible to implant-associated infection, leading to devastating postoperative complications. This implant infection is attributed to bacterial biofilms generating on implant surface, which destroy the surrounding tissue, resulting in implant failure. Since the contaminated medical device surface serves as potential microbial reservoirs causing nosocomial infections, different surface modification methods have been attempted to alter surface chemistry and/or structure of medical devices, endowing them with self-antimicrobial ability. Based on the design principles of antibacterial coatings, the main strategies can fall into two categories: non-release (including anti-adhesion and contact-killing) and antibacterial agent release killing approaches [8]. The release-killing approach consists in putting on the surface of materials inorganic antimicrobial agents such as silver or copper ions [9]. A second approach aims at either inhibiting the adhesion of bacteria on the surface of an anti-adhesion coating or contact-active killing bacteria with light-

activated coatings (e.g. TiO$_2$) or quaternary ammonium polymers [10]. Nonetheless, there are some limitations regarding these approaches, including uncontrollable release rate of the antibacterial agents and a short antimicrobial resistance active time. In response, extensive efforts were made to couple approaches to gain synergistic antibacterial effects to overcome these disadvantages, e.g. by adding anti-bacterial agents into anti-adhesive surfaces [11].

Metal oxides, such as CuO, TiO$_2$ and ZnO, have received much attention as inorganic antibacterial agents against a wide range of bacteria strains [12–14]. MoO$_3$ has found wide applications in semiconductor industry, including gas sensors, oxidative catalyst and photocatalysis [15], due to its unique layered structure and multiple oxidation states. Recently, some researchers have examined the in vitro antibacterial property of various MoO$_3$-based materials against different types of pathogenic bacteria, and relevant mechanisms of antimicrobial activity of those MoO$_3$-based materials are also probed. Zollfrank et al. [1] and Tétault et al. [16] found that the antimicrobial activity of MoO$_3$ particles or sol–gel derived coatings is originating from the in situ formation of oxonium ions (H$_3$O$^+$), enhancing degree of surface acidity with pH value of 4.5–5.5. The diffusion of H$_3$O$^+$ ions into the cell membranes destroys the pH-equilibrium and enzymatic transport systems, thus deteriorating proliferation of bacteria. Krishnamoorthy et al. [17] demonstrated that the MoO$_3$ nanoplates disrupt the bacterial cell wall and thus immediately lead to the cell death. The great advantage of MoO$_3$-based materials is that they do not give rise to drug resistant of bacteria to this bactericidal mechanism. Moreover, invitro cytotoxicity measurements (MTT assays) indicated that MoO$_3$ is safe and harmless to human health due to its non-toxicity [16]. In our previous work, novel the MoO$_3$-SiO$_2$ nanocomposite coating, in which amorphous SiO$_2$ acts as supporting skeletons for antibacterial MoO$_3$ nanocrystalline grains, was prepared on 316L stainless steel, and its antimicrobial properties was shown to kill 80.7% of *E. coli* and 68.9% of *S. aureus* cells [18].

In the present study, to further enhance antibacterial efficacy, an Ag$_2$O-containing MoO$_3$-SiO$_2$ nanocomposite coating was fabricated on Ti–6Al–4V substrate via a double cathode glow discharge technique. The antimicrobial design of the nanocomposite coating combines multiple approaches, such as active release of Ag$^+$ ion (antibacterial agent) and proton, photocatalytic disinfection, as well as anti-adherence of bacterial by hydrophobic surface. The influences of the Ag$_2$O addition on the microstructure, chemical bonding states and photocatalytic property of the as-synthesized nanocomposite coating were characterized using X-ray diffractometer (XRD), X-ray photoelectron spectroscopy (XPS), Scanning electron microscope (SEM), Transmission electron microscopy (TEM), Fourier transform infrared spectroscopy (FTIR), UV–visible spectroscopy and Raman spectroscopy. Four representative microorganisms relevant to nosocomial infection [19,20], including two Gram-negative bacteria (*Escherichia coli* and Salmonella Typhimurium), one Gram-positive bacteria (*Staphylococcus aureus*) and one fungi (*Candida albicans*), were utilized to evaluate the in-vitro antibacterial and antifungal activities for the MoO$_3$-SiO$_2$ -Ag$_2$O nanocomposite coating.

2. Materials and methods

2.1. Coatings preparation

Substrate specimen with dimensions of 20 mm × 10 mm × 3 mm was cut from Ti-6Al-4V rods. Firstly, the substrate specimen was ground by standard metallographic techniques with different grades of abrasive papers to obtain surface roughness about 0.5 μm. Subsequently, the polished substrate specimen was ultrasonically cleaned in acetone, alcohol, and finally dried with cold air. The Ag-free MoO$_3$-SiO$_2$ nanocomposite coating and Ag-containing MoO$_3$-SiO$_2$ nanocomposite coating were deposited by a double cathode glow discharge system [21] employing two targets with stoichiometric ratios of Mo$_{50}$Si$_{50}$ and

Mo$_{47.5}$Si$_{47.5}$Ag$_5$, respectively. In attempts to avoid the negative effect of residual gas on quality of coatings [22], before sputter deposition, the chamber was pumped down to a residual gas pressure of 5×10^{-4} Pa. Substrate specimens were etched by Ar ion bombardment at a potential of −650 V for 20 min to get rid of any contamination from the specimen surface. The working gas was composed of high-purity argon and oxygen, which passed into the chamber by mass flow controllers. The major deposition parameters used were as follows: the pressure of working gas maintaining at 40 Pa with an Ar:O$_2$ flux ratio of 10:1, substrate bias voltage (−400 V) with impulse current (a pulse frequency and a duty cycle set at 1100 Hz and 85%, respectively); target electrode bias voltage (−950 V) with direct current ($\sim 3.6 \times 10^{-2}$ A); distance between targets and substrate of 8.5 mm; a deposition temperature setting at 780 °C and a deposition time of 3 h.

2.2. Coating characterization

2.2.1. Scratching tests

A commercial CSM Revetest scratch tester was used to evaluate the adhesive strength between the coating and the Ti-6Al-4V substrate. During scratching test, a diamond stylus with 0.2 mm tip radius (120° cone angle) was drawn across the coating surface by continuously increasing the normal load at a loading rate of 100 N/min and a scratch velocity of 10 mm/min. The length of total the scratch was 10 mm and the duration of 1 min. The friction force and penetration depth were simultaneously recorded and presented as a function of the displacement of the diamond stylus. The adhesion strength of the coatings can be determined by the signal of penetration depth and friction force, as well as the observation of scratch tracks morphologies.

2.2.2. Microstructural characterization

The phase analysis of the as-received coatings was carried out using an XRD with a D8 ADVANCE diffractometer and XRD data were collected employing Cu-Kα irradiation with a current of 30 mA and a potential of 40 kV. Data was acquired over a 2θ range of 5–70°, with a scan speed of 0.03° per second. SEM observation of the surface and cross-sectional morphologies of the as-synthesized coatings were performed using a field-emission SEM (FE-SEM Hitachi, S-4800, Japan), equipped with an energy dispersive spectrometer (EDS) attachment (EDX-4; Philips). Both TEM plan-view and cross-sectional microstructure observations of the coatings were accomplished by using a JEOL JEM-2010 transmission electron microscope operated at an accelerating voltage of 200 kV. Plan-view and cross-sectional TEM samples were fabricated by a single-jet electrochemical polishing method and a focused ion beam (FIB) microscope (FEI xP200, FEI Company, Hillsboro, OR), respectively. XPS spectra were recorded using an ESCALAB 250 spectrometer analyzer (Thermo VG Co, USA) with an Al Kα X-ray source with an energy of 1486.71 eV. The XPS results were calibrated based on the procedure reported in references [23,24]. FTIR spectra were obtained via a single beam Perkin-Elmer Spectrum GX (RXI, USA) over a wavenumber range from 4000 to 400 cm^{-1} at a resolution of 2 cm^{-1}. Raman analyses were carried out using a Renishaw Raman Imaging Microprobe System 3000 spectrometer operating at an excitation wavelength of 532 nm. The incident laser power and resolution were 5 mW and 2 cm^{-1}, respectively. The wettability of the as-received coatings were measured by a contact angle meter (JC2000C, Powereach, China) at ambient temperature using a volume of 4 μL distill water droplet [25,26].

2.2.3. Photocatalytic activity evaluation

The photocatalytic activities of the as-synthesized coatings were investigated by measuring the photo-degradation of RhB solution at 15 cm apart of the 300 W Xe lamp. During photocatalytic process, the coating samples with a radiation area of 1 mm × 1 mm, which were sealed in a quartz cell, were soaked in a 3 mL RhB solution with the initial concentration of 10 mg L^{-1}. After stirring in dark condition for

1 h to achieve adsorption/desorption equilibrium, the RhB solutions were irradiated with a 300 W Xe lamp for different time intervals and their concentration was determined by using a UV–visible spectrometer through comparing with the standard curve of RhB. UV–vis diffuse reflectance spectra (UV–vis DRS) of the coatings were recorded by using a JASCO V-670 spectrophotometer equipped with an integrating sphere accessory. Photoluminescence (PL) spectra of the tested coatings were measured by an Edinburgh FL/FS900 spectrophotometer with an excitation wavelength of 325 nm.

2.2.4. Antibacterial activity tests

The antibacterial ability of specimens was quantitatively evaluated by the bacterial counting method. Prior to each antibacterial experiment, the samples culture vessel and tubes were sterilized at 121 °C for 30 min with autoclave and then stored in a vacuum desiccator. Three gram bacterial strains (including two Gram-negative bacteria (*Escherichia coli* and Salmonella Typhimurium) and one Gram-positive bacteria (*Staphylococcus aureus*)) and one fungi (*Candida albicans*) were used to analyze the in vitro antibacterial and antifungal activities for the as-deposited coatings. All the gram bacteria strains were cultivated in Luria-Bertani (LB) nutrient solution, incubating on a rotary shaker at shaking speed of 150 rpm at 37 °C for 24 h. *Candida albicans* (*C. albicans*, CCTCC AY 204006, yeast) were cultured in Sabouraud broth medium for 24 h at 37 °C. The cultured bacterial strains were harvested by centrifugation, washed three times by phosphate buffer solution (PBS) to remove any residual culture medium, and finally re-suspended in proper volumes of PBS. The final concentration of bacterial suspension was diluted to contain the cell densities of approximately 1×10^5 colony forming unit (CFU) mL^{-1}. Subsequently, a 100 μL bacterial suspension was placed onto the sample surface and the samples with the bacterial suspension were incubated at 37 ± 0.5 °C for 12 h dark conditions. At the end of the incubation period, each sample was rinsed in PBS and ultrasonically detached in the PBS solution for 5 min. The viable bacteria in the PBS were quantified by standard serial dilution and plate-counting. The bacterial suspension incubated on uncoated Ti-6Al-4V was used as control. Antibacterial rate (R), according to the National Standard of China GB/T 21510-2008, was determined by following expression:

$$R = (A - B)/A \times 100\%$$

where A and B are the average numbers of viable bacterial colonies (cfu/mL) on the uncoated Ti-6Al-4V and the as-deposited coatings, respectively. The viable bacterial were counted according to the National Standard of China GB/T 4789.2 [27]. Prior to SEM observations of bacterial cells, the bacteria were fixed with 2.5% glutaraldehyde solution and then and dehydrated with 60%, 80%, 90% and 100% ethanol for 10 min each.

3. Results

3.1. Structural characterization of the coatings

3.1.1. XRD analysis

XRD patterns obtained from the Ag-free MoO_3-SiO_2 nanocomposite and Ag-containing MoO_3-SiO_2 nanocomposite coatings are presented in Fig. 1. All the diffraction lines of the Ag-free MoO_3-SiO_2 nanocomposite coating can be assignable to orthorhombic structured α-MoO_3 with space group Pbnm, as referred from the JCPDS card no. 05–0508. The diffracted intensities of the {0 k0} reflection planes, such as the (020), (040) and (060) located at 2θ = 12.8°, 25.8° and 39.1°, respectively, are significantly stronger than those of the corresponding standard powder diffraction pattern, indicating that the α-MoO_3 phase exhibits a apparently preferred crystal growth direction along the *b* axis. This highly anisotropic growth of the α-MoO_3 phase is attributed to its peculiar double-layer configuration, where the chains of asymmetrical MoO_6 octahedra are interconnected in intra-layer of each single layer by
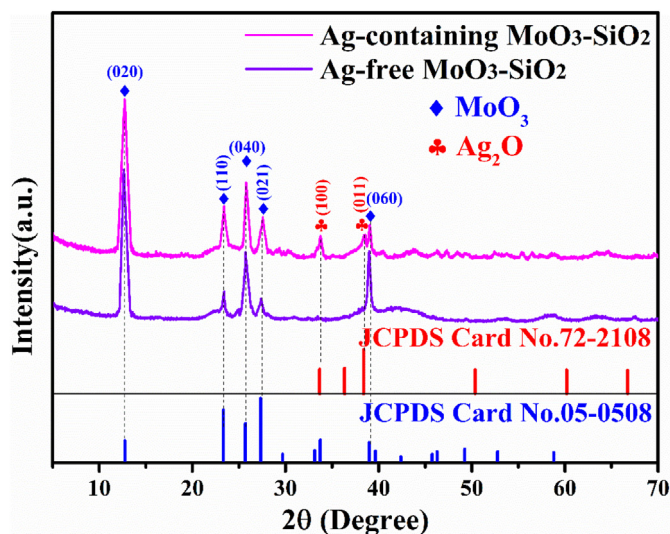

Fig. 1. Typical X-ray diffraction pattern recorded from the Ag-free MoO_3-SiO_2 and Ag-containing MoO_3-SiO_2 coatings.

covalently sharing corner and edge oxygens along the *a* axis and *c* axis directions, and are vertically stacked together in the interlayer through van der Waals forces in the *b* axis direction [28]. For the Ag-containing MoO_3-SiO_2 nanocomposite coating, two weak diffraction peaks at 2θ angles of 33.7° and 38.2° indexed as the (100) and (011) crystallographic planes of hexagonal Ag_2O phase (JCPDS card no. 72–2108), can be detected in addition to the predominant diffraction peaks corresponding to the α-MoO_3 phase. This implies that, after the introduction of Ag, the coating is composed of orthorhombic structured α-MoO_3 as the major phase with small amounts of hexagonal Ag_2O phase. Further, closer examination of the XRD patterns of the two coatings suggested the presence of a diffuse peak over a 2θ range of 21–23° and such a diffuse peak is indicative of the presence of amorphous structured SiO_2 phase.

3.1.2. XPS analysis

In order to disclose the influence of Ag additions on both the valence state and elemental compositional information of the coatings, XPS was performed. As illustrated in the XPS survey spectra (Fig. 2(a)), the signals of C 1s, O 1s, Si 2p, Si 2s, Ag 3d, Mo 3d and Mo3p are clearly observed for the Ag-containing nanocomposite coatings, whereas no XPS characteristic peaks of Ag 3d are detectable for the Ag-free nanocomposite coatings, as expected. The trace amount of C with a binding energy of C 1s centered on 284.6 eV originates from adventitious hydrocarbon layer covering the coating surfaces. As can be seen from Fig. 2(b), Mo3d core-level spectra consist of a doublet peak with a theoretical peak intensity ratio $Mo3d_{3/2}/Mo3d_{5/2}$ of 2/3 and a splitting energy of spin–orbit of 3.2 eV [15]. For the Ag-free nanocomposite coatings, the photoemission line of $Mo3d_{5/2}$ orbital was located at 232.6 eV, confirming that the valence state of Mo element is Mo^{6+} in MoO_3 phase [29]. However, after the addition of Ag, the $Mo3d_{3/2}/Mo3d_{5/2}$ doublet is shifted toward higher binding energy. This is due to the interaction between the oxides of Mo and Ag, leading to charge transfer from Ag^+ to Mo^{6+} ions in the coating [23]. From Fig. 2(c), the measured Si 2p XPS spectra display a single peak located at a binding energy of 102.4 eV, which is characteristic of chemical state of Si in the form of SiO_2 [30]. Combined with the XRD result, it may be suspected that the SiO_2 in the two nanocomposite coatings is characterized by an amorphous structure. Seen from the high-resolution Ag 3d spectrum (Fig. 2(d)), the chemical states of Ag 3d are doublet composed of $3d_{5/2}$ at 368.3 eV and $3d_{3/2}$ at 374.5 eV, respectively, which match well with reported Ag^+ values for Ag_2O oxide [31]. As observed from Fig. 2(e), the broad and asymmetric O1s spectra obtained from the two coatings
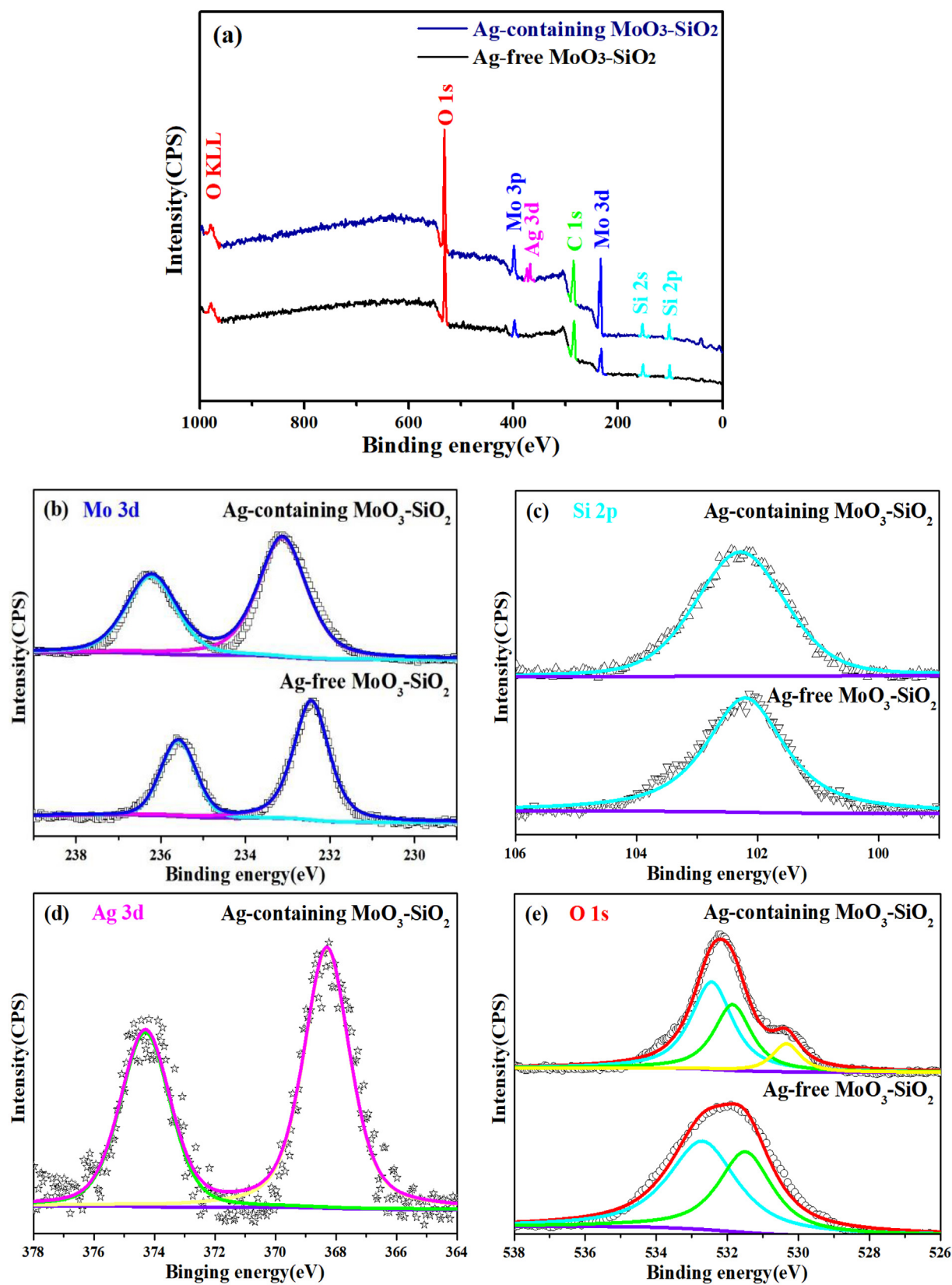
Fig. 2. Typical XPS survey spectra (a) and high-resolution XPS spectra for (b) Mo 3d (c) Si 2p (d) Ag 3d (e) O 1s obtained from the as-deposited Ag-free MoO_3-SiO_2 and Ag-containing MoO_3-SiO_2 coatings.
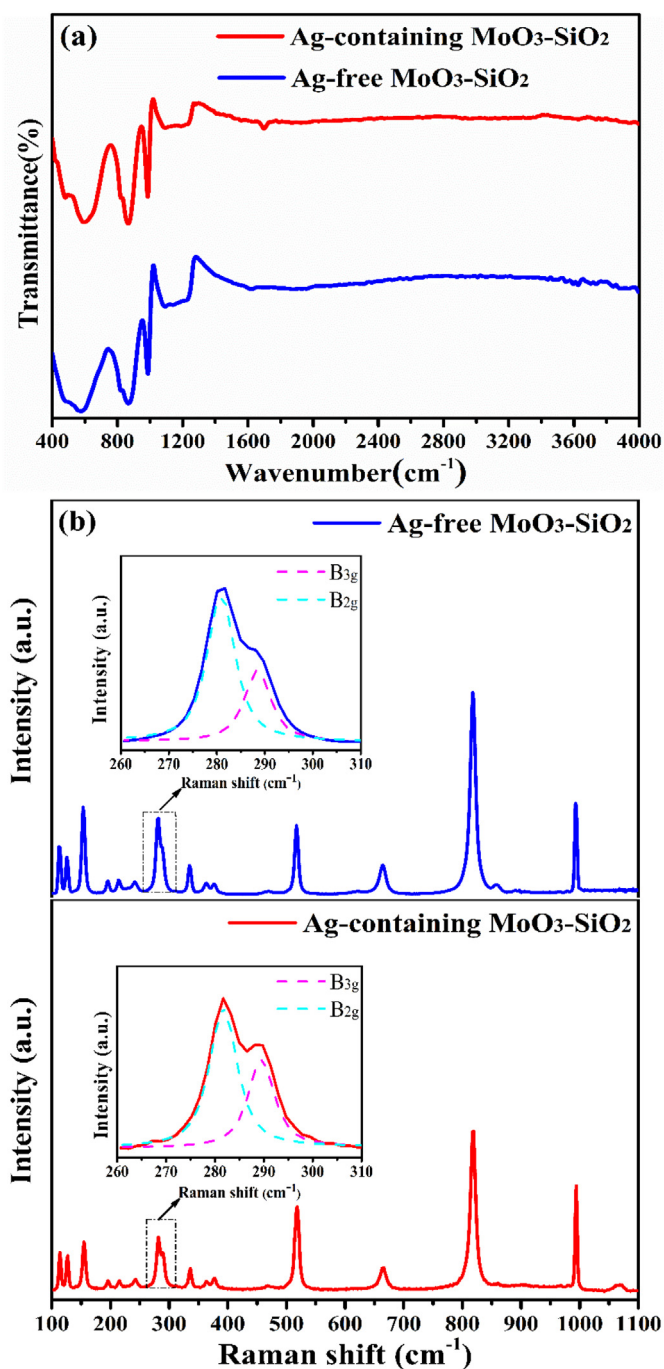
Fig. 3. (a) FTIR spectra and (b) Raman spectra of the Ag-free MoO_3-SiO_2 and Ag-containing MoO_3-SiO_2 coatings.

Raman spectra recorded on the two coatings are illustrated in Fig. 3(a) and (b), respectively. As shown in Fig. 3(a), for the Ag-free MoO_3-SiO_2 coating, it is clear that three distinct characteristic bands in the range of 400–1000 cm^{-1} are associated with Mo−O vibrational interaction: bands at 577.7 cm^{-1} and 866.9 cm^{-1} correspond to the bending vibration of three molybdenum atoms bonded together with the oxygen atoms and stretching vibration of the Mo-O-Mo bridging bonds, respectively, while the band peak located at 986.7 cm^{-1} is assigned to the terminal oxygen symmetric stretching vibration of the Mo=O bond, which is a typically characteristic band of layered structured α-MoO_3 phase [34]. The broad band from 1000 to 1200 cm^{-1} and a weak peak at 440 cm^{-1} originate from stretching and bending vibrations of Si−O−Si, respectively, in conformity with the SiO_2 bond structure [35,36]. Those results are also in agreement with the XRD and XPS analysis. After adding Ag into the coating, the band peaks of α-MoO_3 and SiO_2 undergo little change in the FTIR spectrum. Since the band peaks from 500 to 800 cm^{-1} corresponding to Ag_2O bond vibration are overlapped with those for α-MoO_3, another weak peak at 1696 cm^{-1} belonging to Ag−O bond in Ag_2O is detected [37]. As can be seen from the Raman spectrum of the Ag-free MoO_3-SiO_2 coating (Fig. 3 (b)), Raman peaks centered at 114, 125, 153, 195, 213, 241, 282, 334, 363, 663, 817 and 994 cm^{-1} are related to the α-MoO_3 crystalline phase, and Raman spectrum of α-MoO_3 can be decomposed into the stretching, deformation and lattice vibration modes, corresponding, respectively, to the frequency range of 1000–600 cm^{-1}, 600–400 cm^{-1} and below 200 cm^{-1} [38]. In the low frequency range (< 200 cm^{-1}), the peaks appear at 114, 125, 153 and 195 cm^{-1} are B_{2g} (translational rigid MoO_4 chain), B_{3g} (translational rigid MoO_4 chain), A_g/B_{1g} (δ(O_2 Mo_2)n) and B_{2g} (δ O_2–Mo–O_2 scissor) modes [39], respectively. In the intermediate frequency range, the peaks centered around 213, 241, 282, 334 and 363 cm^{-1} correspond to the A_g(δ O_2–Mo–O_2 scissor), B_{3g}(δ O_2–Mo–O_2 scissor), B_{2g}(δ O_1 = Mo = O_1 wagging), A_g/B_{1g}(δ O_3−Mo−O_3 bending) and B_{1g} (δ O_2 = Mo = O_2 scissoring) modes [34], respectively. In addition, careful inspection shows that the asymmetrical band in the range of 260–300 cm^{-1} can be fitted into two peaks located at 282 and 290 cm^{-1}, ascribed to the modes of B_{2g} and B_{3g}, respectively. In the higher frequency range, the 664 cm^{-1} peak results from the antisymmetric v_{as} Mo−O_2−Mo stretching (B_{2g}/B_{3g} mode), and the peaks of 817 and 994 cm^{-1} are derived from the antisymmetric Mo−O_3−Mo stretching (A_g mode) along the a axis direction and v Mo= O_1 (A_g mode) symmetric stretching vibration with bonding aligning along the b axis direction [40], respectively. Note that the presence of the band at 994 cm^{-1} is supposed to a fingerprint vibration characteristic for layered structured orthorhombic α-MoO_3 [38]. Moreover, the peak near 517 cm^{-1} arises from the symmetrical Si-O-Si vibration mode of amorphous SiO_2 present in the Ag-free MoO_3-SiO_2 nanocomposite coating [41]. In the case of the Ag-containing nanocomposite coating, the appearance of a weak Raman signal at 1072 cm^{-1} assigned to the contribution of Ag−O stretching mode of the presence of Ag_2O phase, is observed, as expected [42]. It should be noted that the intensity ratio of the Raman bands at 282 cm^{-1} (B_{2g}) and 290 cm^{-1} (B_{3g}) reflects local symmetrical changes induced by the generation of oxygen vacancies [43]. After the addition of Ag, the B_{3g} mode is obviously enhanced (the ratio of B_{3g}/B_{2g} = 0.75) in contrast to the Ag-free coating (the ratio of B_{3g}/B_{2g} = 0.64), implying that the Ag addition promote the formation of more oxygen vacancies. Normally, the higher content of oxygen vacancies can excite different metal oxidation states and thus improve the catalytic activities.

3.1.4. SEM and TEM observations

Fig. 4 shows SEM images of the surface and cross-sectional morphologies of the as-synthesized Ag-free MoO_3-SiO_2 nanocomposite and Ag-containing MoO_3-SiO_2 nanocomposite coatings deposited on Ti-6Al-4V substrates, together with the corresponding EDS elemental mapping. As shown in Fig. 4(a), many flake-shaped α-MoO_3 crystals, with dimensions of 3.5 ± 0.4 μm in length, 2.6 ± 0.3 μm in width
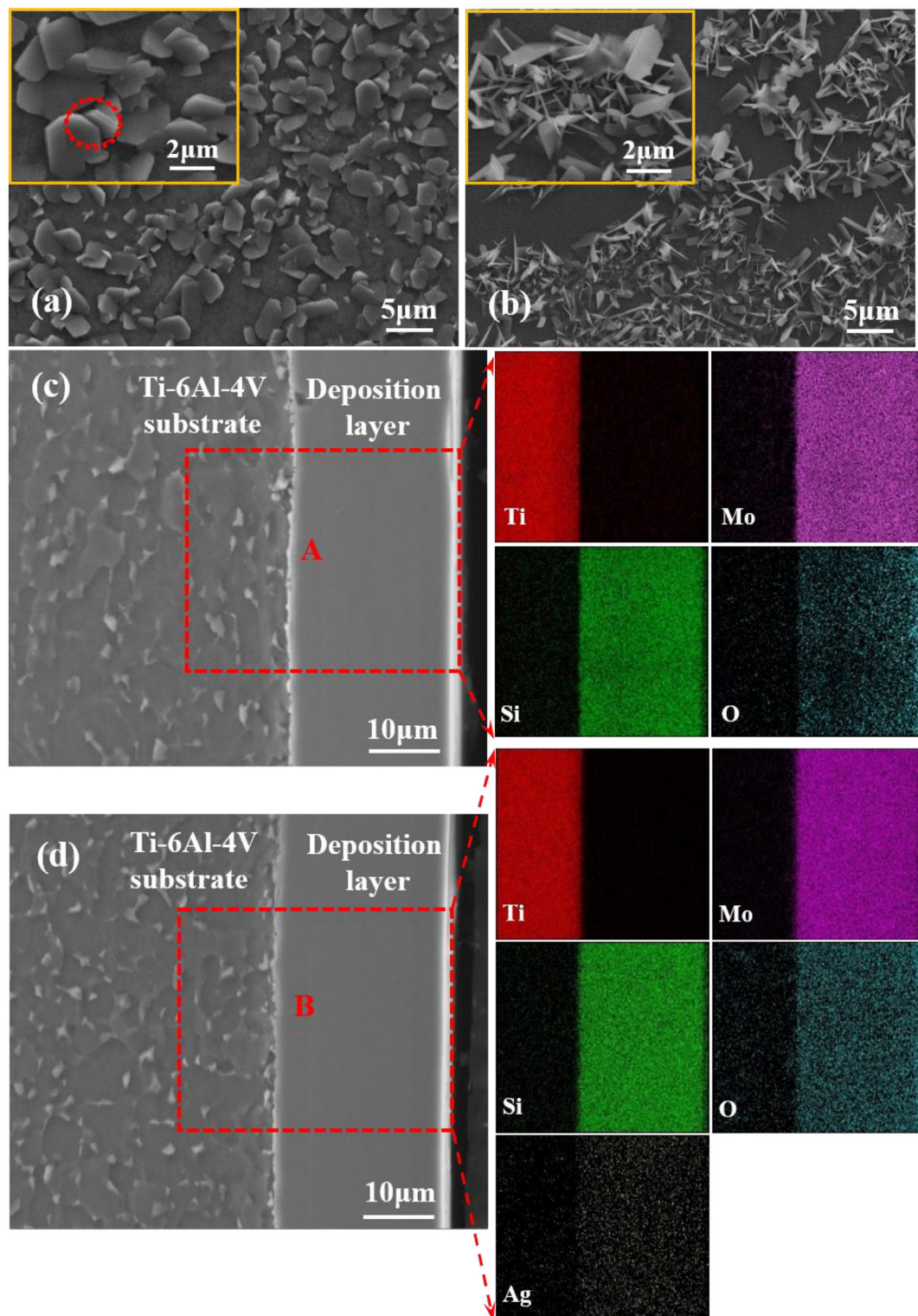
suggest that O element presents at least two chemical states of oxygen species. After decomposition, the O1s peaks for the Ag-free nanocomposite coating are composed of two contributions at 531.85 and 532.48 eV, which are attributed to O^{2-} in MoO_3 and SiO_2, respectively [32]. In the case of the Ag-containing nanocomposite coating, along with the peaks of MoO_3 and SiO_2, a distinguishable shoulder peak is observable at 530.21 eV in the O 1s spectrum, which is assigned to the lattice oxygen in the Ag_2O [33].

3.1.3. FTIR and Raman spectroscopy analysis

To further gain insight into the chemical structures and bond order of the as-synthesized Ag-free MoO_3-SiO_2 nanocomposite and Ag-containing MoO_3-SiO_2 nanocomposite coatings, typical FTIR spectra and

Fig. 4. SEM images of the surface morphologies for (a) Ag-free MoO_3-SiO_2 and (b) Ag-containing MoO_3-SiO_2 coatings; typical cross-sectional images and the corresponding EDS elemental maps for (c) Ag-free MoO_3-SiO_2 and (d) Ag-containing MoO_3-SiO_2 coatings.

and 300 ± 20 nm in thickness, grow mostly parallel to the surface of the Ag-free coating, and a few α-MoO_3 flakes are interlinked with each other at edges due to high deposition temperature used here. The ends of these α-MoO_3 flakes show triangular in shape, stemming from the difference in stacking rates of MoO_6 octahedrons in the [100] and [001] directions. Since the Mo−O covalent bonds are stronger in the c-axis direction than in the a-axis direction, the growth of α-MoO_3 flakes

along the [001] direction is energetically more favorable, and the hexagonal flakes are stretched along c-axis direction, resulting in a triangular-shape tip on the ends [44]. Furthermore, step-like pattern (highlighted by red circles in the inset of Fig. 4(a)) is observed on the edges of α-MoO_3 flakes, which originates from aggregating two adjacent flakes to form a layered structure along [010] direction [40]. As can be seen from Fig. 4(b), after the addition of Ag, some α-MoO_3
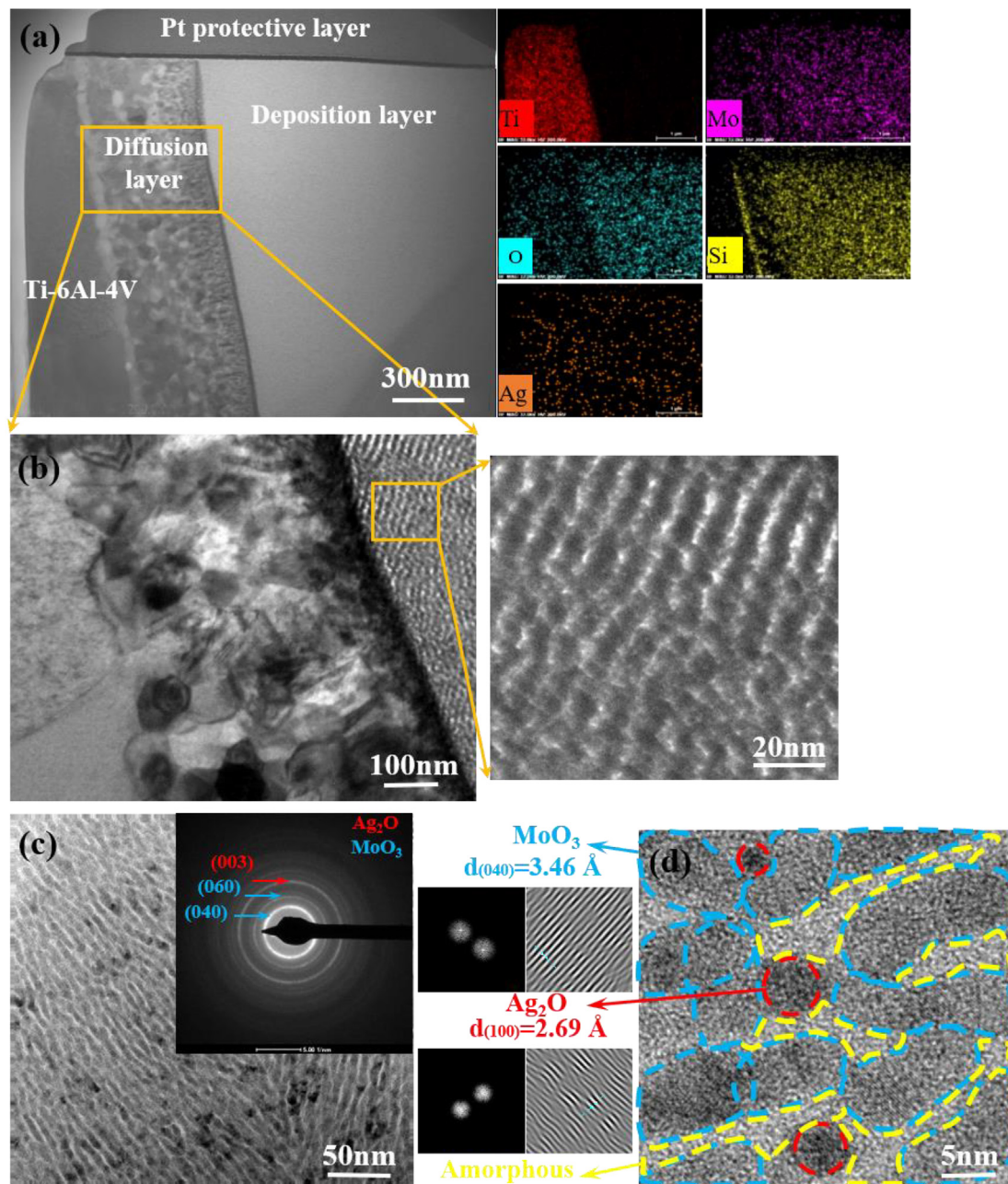
Fig. 5. (a) The typical cross-sectional TEM micrographs with the corresponding EDS elemental mapping and (b) the high-magnification bright-field TEM micrograph taken from interfacial region between the Ti-6Al-4V substrate and Ag-containing MoO_3-SiO_2 coating. (c) The plan-view TEM bright field image and (d)the high-resolution TEM image of Ag-containing MoO_3-SiO_2 coating.

flakes, growing approximately vertically to the surface of the Ag-containing coating, look like thin strips. The average three dimensional sizes of α-MoO_3 flakes are reduced to 2.8 $\pm$ 0.5 μm in length, 1.3 $\pm$ 0.2 μm in width and 260 $\pm$ 8 nm in thickness, denoting that Ag addition alters the arrangement and size of α-MoO_3 flakes. These α-MoO_3 flakes on the two coating are derived from growing outward from the coatings surface during sputter deposition. From the cross-sectional morphologies (Fig. 4(c) and (d)), both the Ag-free and Ag-containing MoO_3-SiO_2 nanocomposite coatings exhibit dense and uniform microstructure with a thickness of ~22 μm and adhere intimately to Ti-6Al-4V substrate, free of micro-cracks or voids existing at both the entire coatings and interfacial region between nanocomposite coating and substrate. From the EDS elemental mapping of the selected regions shown in Fig. 4(c) (indicated by A) and Fig. 4(d) (indicated by B), the entire coatings are visualized in the mapping images of Mo, Si, O and

Ag (for the Ag-containing coating), and the spatial distribution of these elements are homogeneously dispersed across the coating thickness, demonstrating that the coatings exhibit a formation of uniform microstructure.

To further reveal the microstructural characteristics of nanocomposite coatings and the interface between nanocomposite coating and substrate, both cross-sectional and plan-view TEM micrographs of the Ag-containing MoO_3-SiO_2 nanocomposite coating were acquired. Typical TEM cross-sectional view and the corresponding EDS elemental mapping obtained from interfacial region between nanocomposite coating and substrate are shown in Fig. 5. From the TEM cross-sectional image, three distinct regions with a marked contrast difference are discerned from Fig. 5(a): a coarse grained Ti-6Al-4V substrate on top which exists a ~600 nm thick diffusion layer and then a dense and fine grained Ag-containing MoO_3-SiO_2 deposition layer. A high-

magnification bright-field TEM micrograph (Fig. 5(b)) indicates that the intermediate diffusion layer consists of fine equiaxed grain structure with an average grain size of 100 nm and the deposition layer is characteristic of cellular grains structure, with a homogeneous distribution of grain size in the range of about 12 nm in cross-section. Both the interfaces of Ti-6Al-4V substrate/diffusion layer/deposition layer exhibit a good adherence. EDS elemental mapping images show that the diffusion layer is predominantly enriched in Ti, Mo and Si with only small amounts of O and Ag. Such chemical composition and microstructure features of the diffusion layer may provide good adhesion strength between the Ag-containing MoO_3-SiO_2 deposition layer and the substrate. Representative plan-view bright field TEM and high resolution TEM (HRTEM) micrographs obtained from the Ag-containing MoO_3-SiO_2 deposition layer, along with the corresponding selected area diffraction (SAD) pattern are shown in Fig. 5(c) and (d). It is evident that three different contrast regions can be observed in plan-view image of the deposition layer (Fig. 5(c)). SAD pattern exhibits ring and diffused halo diffraction pattern (amorphous halo is not shown due to the use of a beam stop), indicating that the microstructure of the coating consists of a mixture of amorphous and polycrystalline structures. Two strong rings are closely indexed as the (040) and (060) lattice planes of α-MoO_3 phase, while a weak ring corresponding to the (003) plane of Ag_2O phase is weakly present. The result further confirms a preferred (020) texture for α-MoO_3 phase, in agreement with the XRD analysis. As can be seen in HRTEM image (Fig. 5(d)), in the equiaxed gray contrast region (indicated by dotted blue line), interplanar spacing was measured to be 0.346 nm, which was consistent with the (040) lattice spacing of α-MoO_3 phase, while in the near-spherical dark contrast region (indicated by dotted red line), parallel line fringes with a spacing of 0.269 nm can be assigned to the (100) crystallographic plane of hexagonal Ag_2O phase. The two crystalline phases are dispersed at the nano-scale and evenly embedded in an amorphous phase.

3.2. Scratch tests and water contact angle measurements

Scratch tests were carried out on the as-deposited Ag-free and Ag-containing MoO_3-SiO_2 nanocomposite coatings to evaluate qualitatively the adhesion strength between the coatings and Ti-6Al-4V substrates. During the scratch measurements, the adhesion characteristics of the coatings are described by two critical loads (i.e. at the L_{c1} and L_{c2} points), where L_{c1} and L_{c2} are defined as the minimum loads required to initiate micro-cracks in the coating and to strip the coating from a substrate completely, respectively [45,46]. Commonly, L_{c1} is determined by careful examination of the scratch morphology, because the friction force curves are quite insensitive to local cracking events within the coating. Fig. 6 shows typical tangential friction force and penetration depth as a function of normal force for the two coatings. As observed from Fig. 6, at an early stage of the scratch test, the friction force and penetration depth rise slowly, and when the normal forces increase to 49 N and 53 N, a sharp rise in tangential friction force and the penetration depth are easily identifiable, indicating that the L_{c2} values for the two coatings have been attained. During the initial stages of the scratch test, the scratch grooves are very smooth without appreciable damage. Subsequently, the width of scratch grooves and the degree of plastic deformation created by the sliding indenter increase as the normal load increased. When the normal load is increased to L_{c1} (25 N for the Ag-free coating and 33 N for the Ag-containing coating), the tensile stresses developed at the rear of the sliding indenter are high enough to induce radial cracks, which are aligned perpendicular to the scratch direction. EDS analysis (insets in Fig. 6) was performed in the scratched region corresponding to L_{c1} and the results showed that no Ti signal from substrate was detected. With a further increase in the normal load, the density of the cracks increases, and chipping of the coating appears at the edges of the scratch tracks. When the critical load L_{c2} is reached for both coatings, the indenter has penetrated much of the coating thickness and the coatings exhibit continuous spallation so

that the underlying substrate is exposed. EDS elemental mapping images of the scratch tracks indicate that strong Ti signal is observed in the detached region without detected Mo and Si elements from the coatings, further providing a proof of complete removal of the coatings. It is evident that the Ag-containing coating exhibits higher adhesion strength and greater crack initiation load than the Ag-free coating, suggesting that Ag addition improves the load bearing capacity of the MoO_3-SiO_2 nanocomposite coating.

To assess the surface wettability of the two coatings, the contact angles were measured and each sample was measured at five different points and then averaged, as shown in Fig. 7. The measured water contact angle for the Ag-free MoO_3-SiO_2 and Ag-containing MoO_3-SiO_2 coatings are 115° ± 2.2° and 118° ± 2.5°, respectively, both of which are obviously higher than that of bare Ti-6Al-4V (62° ± 1.6°). This indicates that both coatings display better hydrophobic property than bare Ti-6Al-4 V. In comparison with the bare Ti-6Al-4 V, the higher hydrophobicity provides the two coatings with greater capability to inhibit bacterial adhesion [8].

3.3. Photocatalytic activity

The optical absorption characteristics of a material play an important part in determining its photocatalytic performance. To evaluate optical response for the as-prepared Ag-free and Ag-containing MoO_3-SiO_2 nanocomposite coatings, the UV–vis DRS of the two coatings were measured, as illustrated in Fig. 8(a). As can be seen from Fig. 8(a), the optical absorption spectra resemble each other in shape with a long tail extending into visible region, suggesting that both coatings exhibit strong visible light absorption ability over a broad absorption band from 200 to 800 nm. The presence of Ag_2O phase makes a red shift of absorption edge toward visible region and improves visible light absorbility of the MoO_3-SiO_2 nanocomposite coating. Owing to its photosensitive properties and narrow band gap (~1.3 eV), nanoscale Ag_2O phase can be readily photo-reduced to form Ag by capturing photogenerated electrons under light irradiation. Hence, such a red shift of absorption edge may be attributed to the strong surface plasmon resonance (SPR) effect of the coexistence of Ag_2O and Ag in Ag-containing MoO_3-SiO_2 nanocomposite coating [47].

PL emission spectrum is usually applied to measure the photoactivity of photocatalyst by evaluating the recombination performance of the photo-generated electron-hole pairs [48]. Fig. 8(b) shows the typical PL spectra of the as-prepared Ag-free and Ag-containing MoO_3-SiO_2 nanocomposite coatings recorded in the wavelength range of 420–600 nm at 325 nm wavelength excitation. It is clear that the shapes of PL spectra for the two coatings are similar, but their PL intensities are different. Two main emission peaks located at ~470 nm and ~530 nm can be ascribed to the band-edge recombination of electron–hole pairs. Moreover, some small emission peaks are attributed to the presence of surface defects due to the radiative decay of self-trapping excitation [49]. The PL spectrum intensity of the nanocomposite coating is decreased with the introduction of Ag_2O phase, suggesting that the Ag-containing coating shows much lower recombination rate of the photoexcited electron-hole and thus prolongs the life time of the photogenerated charge carriers. Additionally, the presence of defects in the two coatings is also in favor of an extension of the electron-hole pair life time, because they act as photo-induced charge traps.

To investigate the photocatalytic performance of the as-prepared Ag-free and Ag-containing MoO_3-SiO_2 nanocomposite coatings, the photodegradation of RhB dye solution mixed with the two coatings used as photocatalysts was performed under visible light irradiation and the results are displayed in Fig. 9. As shown in Fig. 9(a) and (b), the characteristic absorption peak of RhB solution at 554 nm, corresponding to n → π* transition of C=O and C=N groups [50], is diminished gradually in intensity with increasing irradiation time for both coatings. Meanwhile, the color of the dye (inset photographs of Fig. 9(a) and (b)) converts from rose red to colorless after irradiation
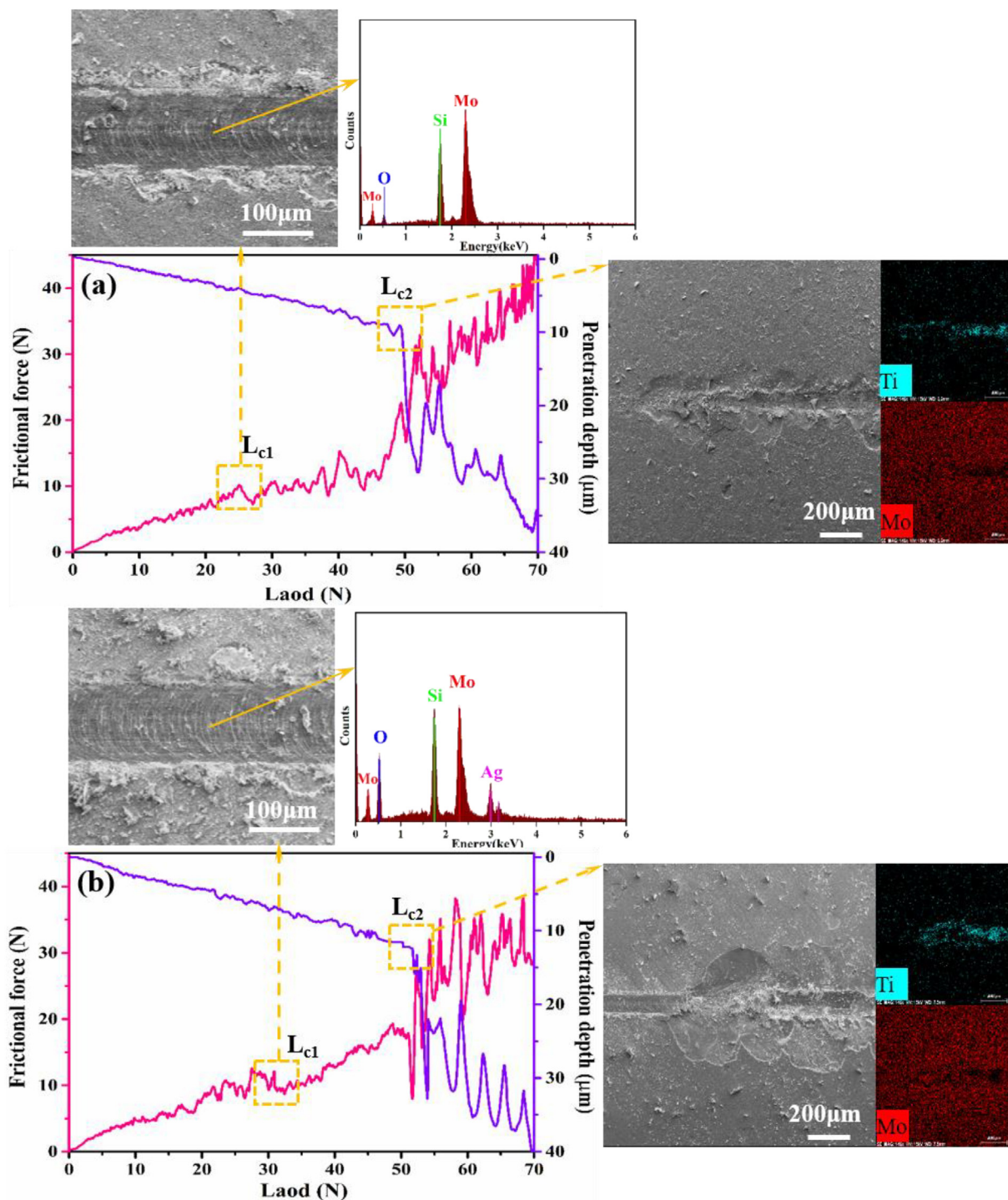
Fig. 6. Typical tangential friction force and penetration depth as a function of normal force for (a) Ag-free MoO$_3$-SiO$_2$ and (b) Ag-containing MoO$_3$-SiO$_2$ coatings. The orange arrow marks the SEM images of the scratch tracks morphologies with the corresponding EDS of the scratch tracks at the point of L$_{c1}$ and L$_{c2}$, respectively.

time of 180 min. The decrease in the peak intensity for the Ag-containing coating is more obvious than that for the Ag-free coating, demonstrating that the introduction of Ag$_2$O phase significantly enhances the degradation of RhB of the MoO$_3$-SiO$_2$ nanocomposite coating. Fig. 9(c) displays the variation of the concentration ratio of C/C$_0$ (C$_0$ and C correspond to initial concentration and the concentration obtained after different irradiation time) as a function of irradiation time for blank contrast and the two coatings. The blank reference tests suggest that the direct photolysis of RhB molecules without catalyst is negligible, denoting that the self-degradation of RhB molecules under

visible radiation hardly occurs. After 180 min irradiation, the degradation percentages of RhB dye are 57% and 88% for the Ag-free and Ag-containing MoO$_3$-SiO$_2$ nanocomposite coatings, respectively. Hence, the Ag-containing coating exhibits much greater photocatalytic activities than the Ag-free coating. Furthermore, the photocatalytic degradation of RhB dye follows a pseudo-first-order kinetics and the reaction rate constant of k can be calculated by the following expression: $\ln(C_0/C) = kt$, where k and t are the photocatalytic first-order reaction rate constant and the irradiation time [51], respectively. After fitting the curves of $\ln(C_0/C)$ versus irradiation time (t) for the two coatings, it
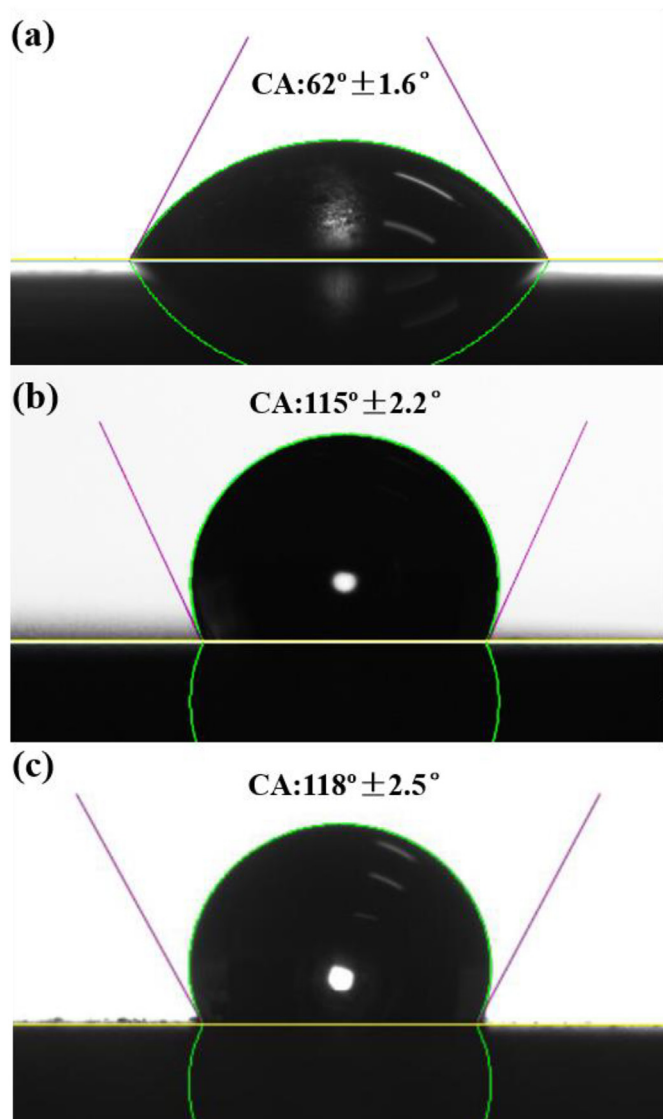
Fig. 7. The photographs of water droplets on (a) the Ti-6Al-4V (b) the Ag-free MoO$_3$-SiO$_2$ and (c) the Ag-containing MoO$_3$-SiO$_2$ nanocomposite coatings.

Fig. 8. UV–vis diffuse reflectance spectra (a) and Photoluminescence spectra (b) of the Ag-free MoO$_3$-SiO$_2$ and Ag-containing MoO$_3$-SiO$_2$ nanocomposite coatings.

is found that the value of ln(C$_0$/C) is linearly proportional to irradiation time (t) (R^2 > 0.96), confirming that the photocatalytic reactions match the pseudo-first-order kinetics. For the degradation of RhB dye by the Ag-containing coating, the k value is determined to 0.0115 min^{-1}, which was larger than that of the Ag-free coating (0.0042 min^{-1}), implying an enhanced photocatalytic activity.

In the case of the Ag-free nanocomposite coating, when the MoO$_3$ was irradiated by visible light, the MoO$_3$ absorbs light to form electron-hole pairs by exciting electrons from the valence band (VB) to the conduction band (CB). The photo-generated electrons in CB react with oxygen molecule in H$_2$O and H$^+$ to produce H$_2$O$_2$ [52]. Meanwhile, the photogenerated holes in VB react with surface hydroxyl group to yield active hydroxyl radicals [53]. These reactive radicals and photo-generated holes, acting as the major active species, are responsible for decomposition of RhB dye under visible light irradiation condition. For the Ag-containing MoO$_3$-SiO$_2$ nanocomposite coating, well dispersed fine Ag$_2$O grains around the MoO$_3$ grains can capture electrons effectively, preventing electrons and holes from recombination. As mentioned above, SPR effect of the coexistence of Ag$_2$O and Ag can promote the harvest of visible light. Alternatively, both the conduction band (CB, 0.14 eV) and valence band (VB, 1.44 eV) of Ag$_2$O lie above that of MoO$_3$(CB,0.31 eV, and VB,3.08 eV) [54]. Hence, a well matched band
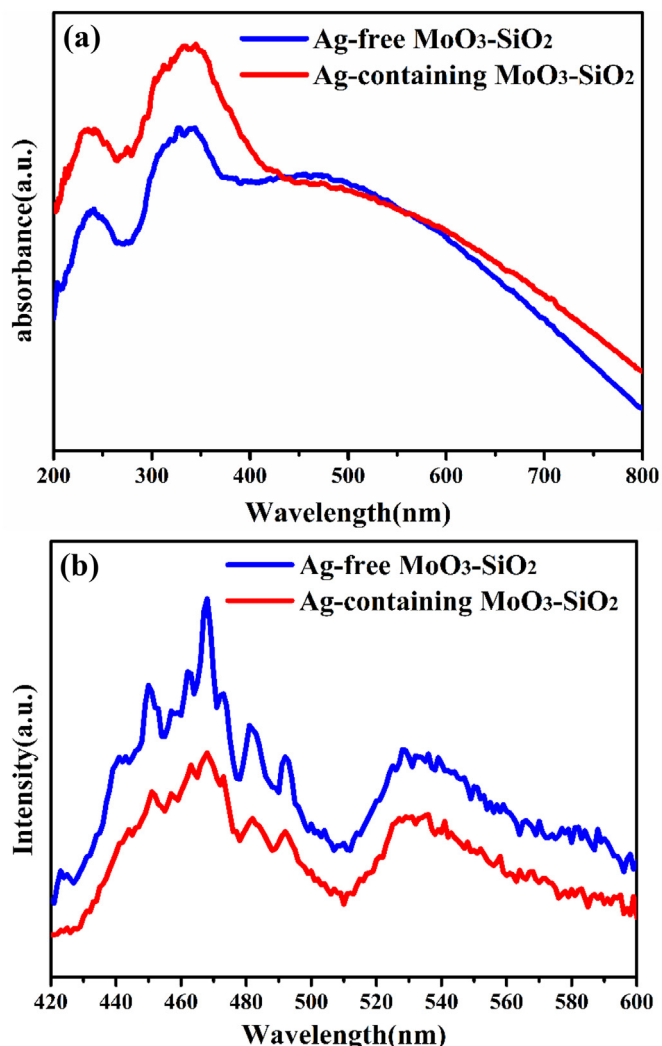
gaps and positions between Ag$_2$O and MoO$_3$ might be favorable for the formation of Ag$_2$O/MoO$_3$ heterostructure. The heterostructure is beneficial to migration of photogenerated carriers and consequent prolongs lifetime of electron-hole pair. Therefore, after the introduction of Ag$_2$O, the Ag$_2$O/MoO$_3$ heterojunction combined with SPR effect endowed by the presence of nanoscale Ag phase may enhance photocatalytic performance for Ag-containing MoO$_3$-SiO$_2$ nanocomposite coating.

3.4. Antibacterial activity

The antibacterial activity of the as-prepared Ag-free and Ag-containing MoO$_3$-SiO$_2$ nanocomposite coatings under both dark and visible light conditions are examined by using two Gram-negative bacteria (*Escherichia coli* and Salmonella Typhimurium), one Gram-positive bacteria (*Staphylococcus aureus*) and one fungus (*Candida albicans*) as representative model bacteria. Fig. 10(a)–(d) presents the photos of agar plates showing the colonies of *Escherichia coli*, Salmonella Typhimurium, *Staphylococcus aureus* and *Candida albicans* grown on the two coatings and the reference Ti-6Al-4V as a function of culture duration under both dark (Fig. 10(a)–(c)) and visible light conditions (Fig. 10(d)). Regardless of under dark or visible light conditions, all the four microorganisms tested are capable of surviving on the surface of uncoated Ti-6Al-4V and the colonies populations of bacterial cells remain virtually unchanged even after 12 h incubation, suggesting that
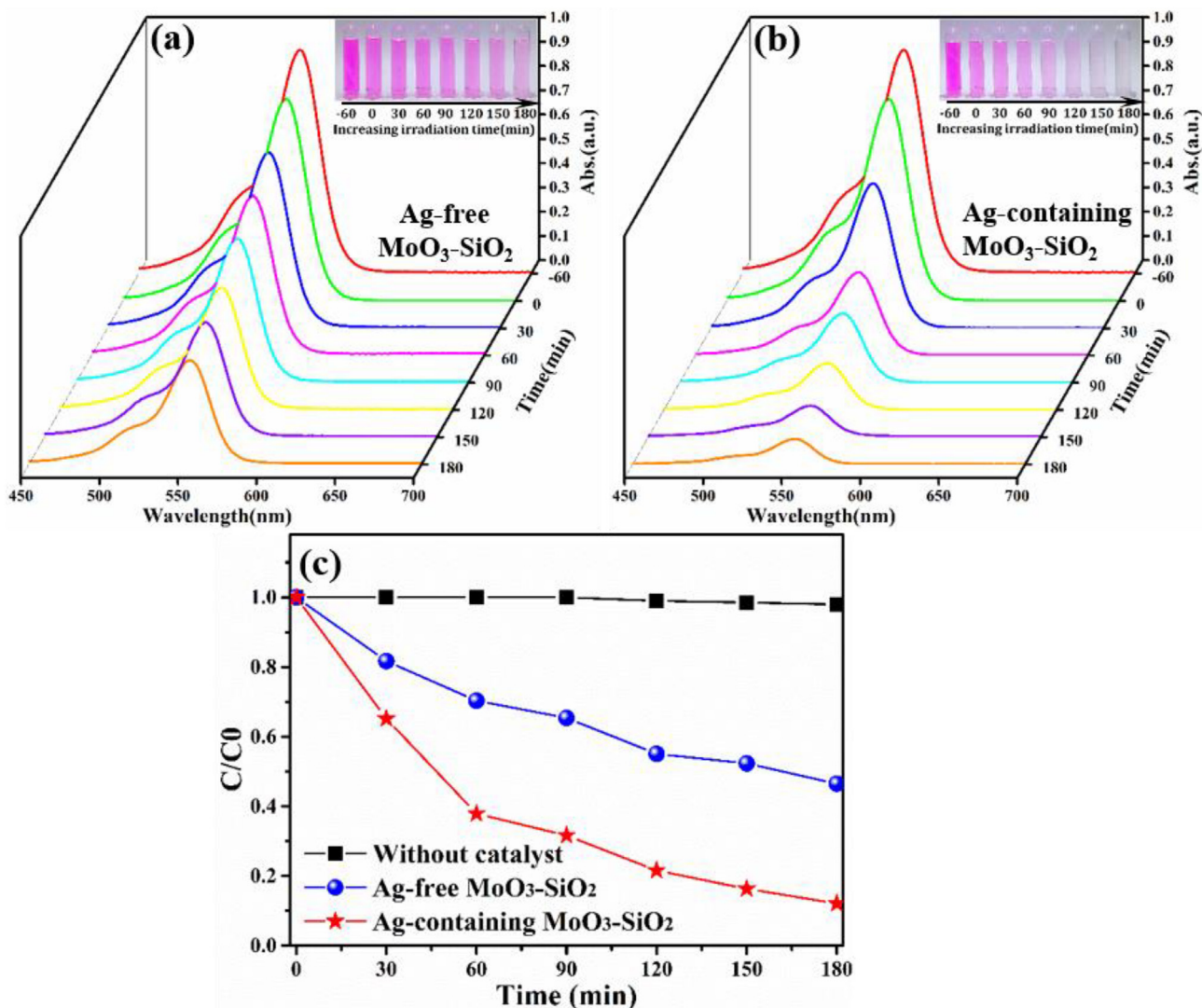
Fig. 9. UV–vis absorption spectra of RhB solution to different irradiation time over (a) the Ag-free MoO$_3$-SiO$_2$ and (b) the Ag-containing MoO$_3$-SiO$_2$ nanocomposite coatings. (c) Photocatalytic degradation curves of RhB solution over different photocatalysts.

bare Ti-6Al-4V has no effect on the inactivation of four bacteria under both dark and visible light conditions. In contrast, the numbers of detectable colonies for the four bacteria grown on the two coatings are found to significantly decrease with increasing incubation time, especially under visible light condition. After 12 h incubation the bacteria colonies die due to the toxicity of the substrate and are no longer observed within the dish. The results suggest that the two coatings can suppress the growth of four bacteria under both dark and visible light conditions and they exhibit a higher antimicrobial activity against the four bacteria under visible light condition. A point worth emphasizing is that the effect of crystal structure of MoO$_3$ on its antimicrobial properties is inconsistent. Zollfrank et al. [1] found that the antimicrobial activity of MoO$_3$ showed a significant decrease after treated at 500 °C, and they attributed this to the increased orthorhombic structured MoO$_3$. On the contrary, Lorenz et al. [55] reported that excellent antibacterial effect against strains of *Staphylococcus aureus*, *Escherichia coli* and *Pseudomonas aeruginosa* was achieved only for the crystallization of MoO$_3$ after annealing at 450 °C. Our previous [18] and present studies have shown that both the hexagonal-structured and orthorhombic structured MoO$_3$ exhibited good antimicrobial ability against Gram-positive (*S. aureus*) and Gram-negative (*E. coli*) bacteria and the orthorhombic structured MoO$_3$ showed a higher antimicrobial activity than the hexagonal-structured one. Furthermore, Singh et al.

[49] indicated that the orthorhombic structured MoO$_3$ exhibited better photocatalytic activity than the hexagonal-structured MoO$_3$ for photodegradation of MB dye. This also offers indirect evidence for the enhanced antimicrobial efficiency of the coatings under illumination with UV radiation.

Fig. 11 shows the antibacterial efficiencies of four bacteria by the two coatings and the reference Ti-6Al-4V after different incubation times under both dark and visible light conditions. As presented in Fig. 11(a–f), the Ag-free coating can completely inactivate four bacterial cells for 12 h (Fig. 11. (a)–(d)) and 6 h (Fig. 11(e)) without and with visible light irradiation, respectively; whereas, after the introduction of Ag$_2$O phase, three Gram bacterial cells (*Escherichia coli*, Salmonella Typhimurium and *Staphylococcus aureus*) are entirely killed after they are incubated for 9 h (the fungicidal rate of 95.5% against *Candida albicans*) and 1 h under visible light conditions (Fig. 11(f)), respectively. This suggests that the Ag-containing coating possesses the better bactericidal ability than the Ag-free coating under both dark and light conditions. Under dark condition, the antibacterial rates of the Ag-free coating against Gram-negative microorganisms are much faster than that of the Ag-free coating against Gram-positive microorganisms during the initial 6 h of culture duration. The disparity in antibacterial rates is largely due to the fact that cell wall of *S. aureus* is characteristic of a three-dimensional spatial network structure with high mechanical
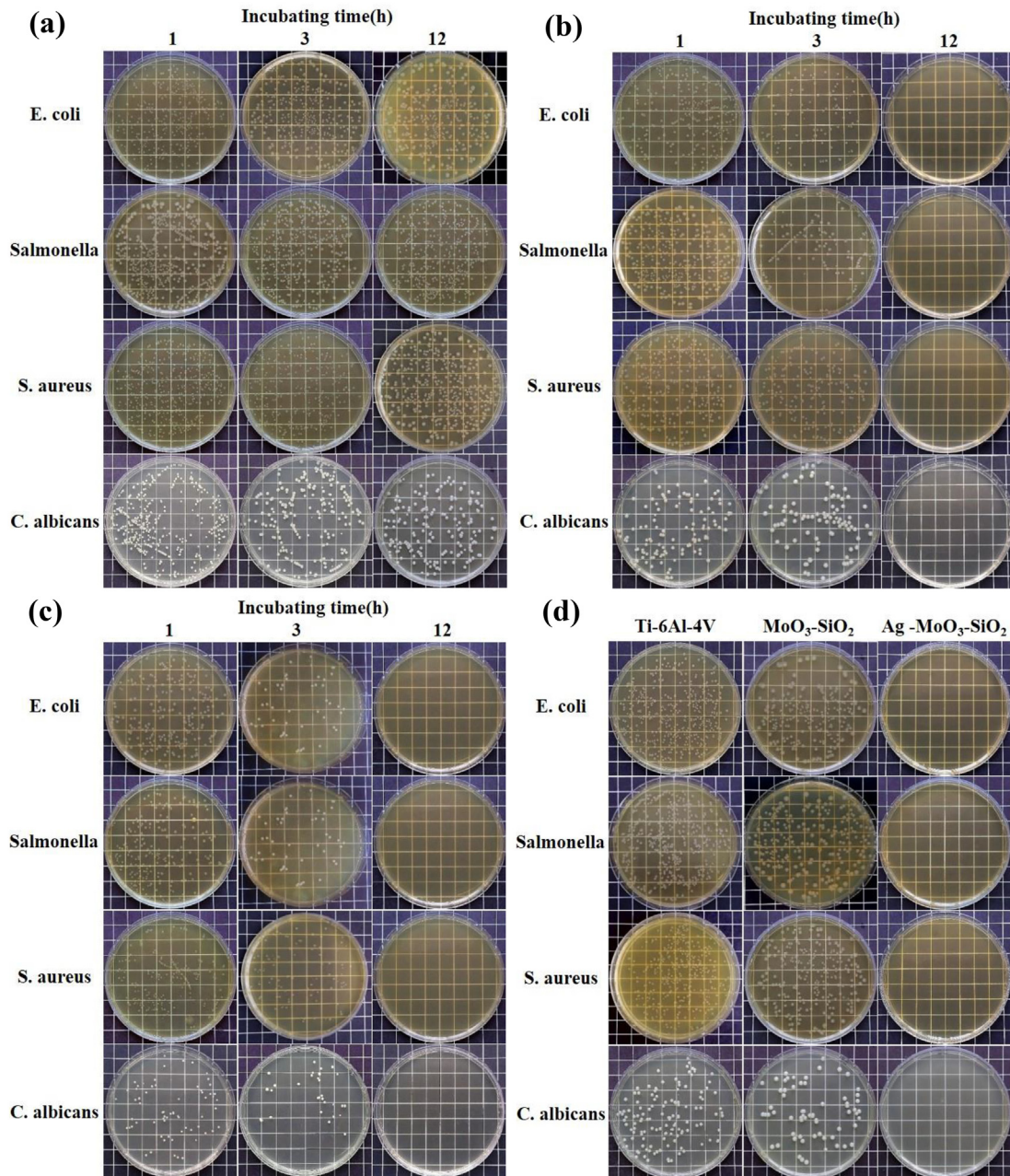
Fig. 10. The photos of agar plates inoculated with four bacterial suspension: (a) Ti-6Al-4V, (b)Ag-free MoO₃-SiO₂ and (c) the Ag-containing MoO₃-SiO₂ coatings after different incubation time (1 h, 3 h, 12 h) without light and (d) after incubate 1 h under visible light condition.

strength, which is harder to be invaded by the antibacterial agents; whereas, Gram-negative microorganisms, such as *E. coli*, has a thin single peptidoglycan layer of plate mesh, which is more susceptible to attack by the antibacterial agents [56]. However, the antibacterial rate of the Ag-containing coating against *S. aureus* increases noticeably, because the proteins of cell membranes for *S. aureus* make it more vulnerable to becoming potential targets assaulted by Ag⁺ ion [57]. Besides, the longer duration required to completely eradicate *C. albicans* may initiate from rigid cell walls containing chitin, ensuring them to survive in aggressive conditions [58]. Nonetheless, in contrast with the results obtained from under dark condition, both the coatings exhibit a higher fungicidal activity against *C. albicans* with visible light irradiation. Presumably, the oxidative activity of reactive oxygen species (ROS) produced by photocatalytic processes exacerbates cells envelope injuries of *C. albicans*. According to the results documented in the literature, the antibacterial activity of the Ag-containing coating, against

Gram-negative bacteria, Gram-positive bacteria and fungi is comparable to that of the TiO₂/Ag₂O composites [33] and Ag containing hydroxyapatite coatings [59], but is significantly higher than that of Ag₂O/TiO₂ nanobelts [60], MoO₃ coating [16] and TiO₂ nanotube-Ag₂O arrays [57].

4. Discussion

To shed light on the antibacterial mechanism of the Ag-containing coating, we compared the SEM morphologies images of four bacteria incubated on the surfaces of the two coatings and uncoated Ti-6Al-4V for 1 h by SEM observation, as shown in Fig. 12. Obviously, the cell morphologies of four bacteria incubated on bare Ti-6Al-4V maintain their respective original cellular morphologies, evidenced by well-preserved and smooth cell wall. This result suggests that it is safe to bacterial cells in direct contact with bare Ti-6Al-4V, since bare Ti-6Al-4V
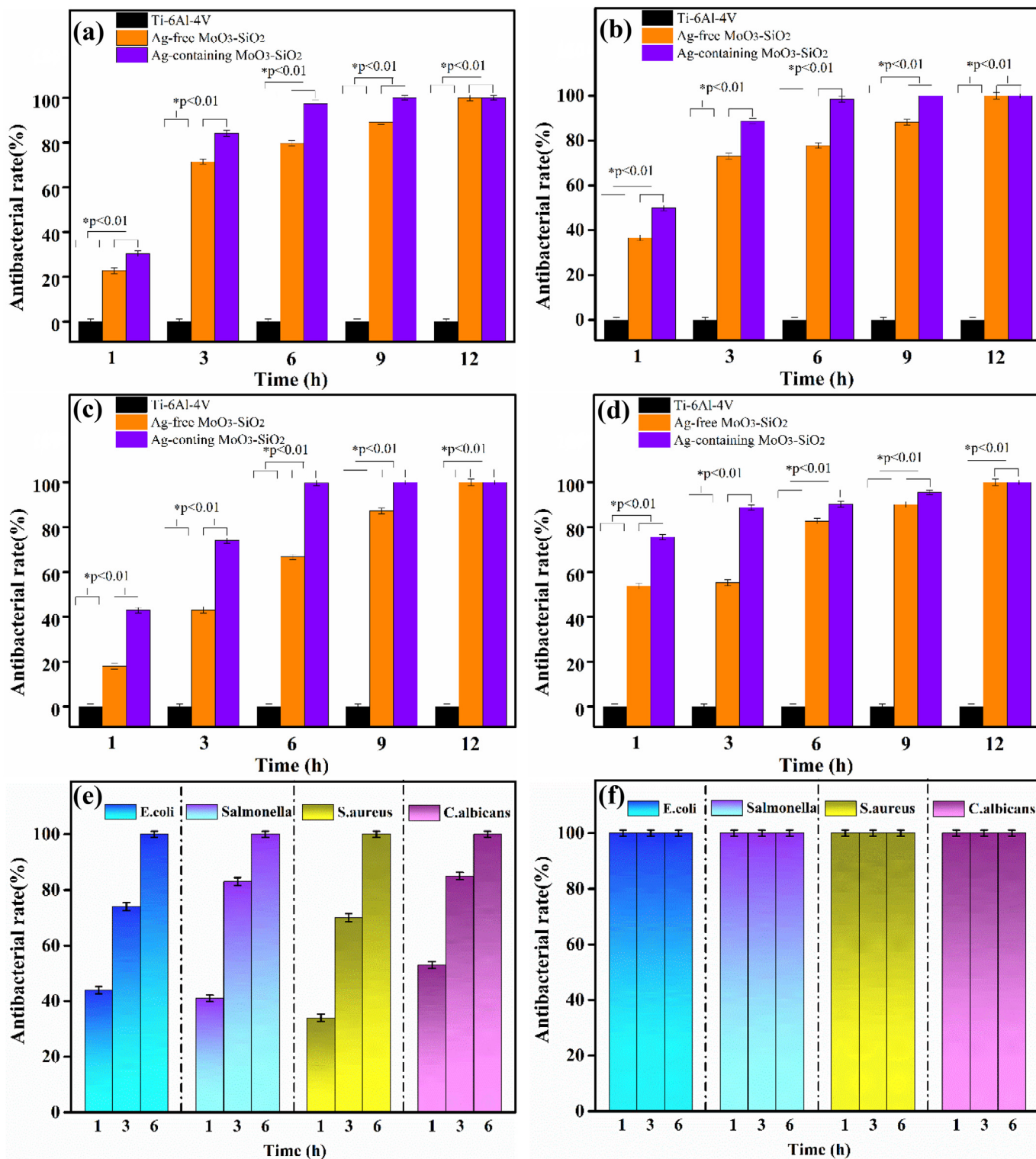
Fig. 11. Antibacterial rate diagram of the uncoated Ti-6Al-4V, the Ag-free MoO$_3$-SiO$_2$ and Ag-containing MoO$_3$-SiO$_2$coatings after different incubation times (1 h, 3 h, 6 h, 9 h, 12 h) in (a) *Escherichia coli*, (b) Salmonella, (c) *Staphylococcus aureus* and (d) *Candida albicans* bacterial suspension under dark condition. Antibacterial rate diagram of (e)Ag-free MoO$_3$-SiO$_2$ and (f) Ag-containing MoO$_3$-SiO$_2$ coatings exposed to visible light. Error bars indicate the standard deviation from at least triplicate experiments ($n \geq 3$).

has virtually no bactericidal effects on the four bacteria even under visible light irradiation condition. In contrast, after four bacteria contacted with two coatings, the bacteria undergo obvious cell- membrane lesions of varying degrees, disrupting cellular integrity. Under dark condition, many grooves and pits can be observed on the cell wall of bacteria on both coatings, and slight distorted and wrinkled surfaces

appear at these cell membranes, indicating that both coatings a negative impact on the integrity of bacterial cell membranes. As noted earlier, the biocidal effect of MoO$_3$ stems from the formation of H$_3$O$^+$ through surface acidic reaction, and subsequently the release of H$_3$O$^+$ penetrating into the cell membranes results in disruption of enzymatic transport systems and limitation of metabolic activities [55]. This
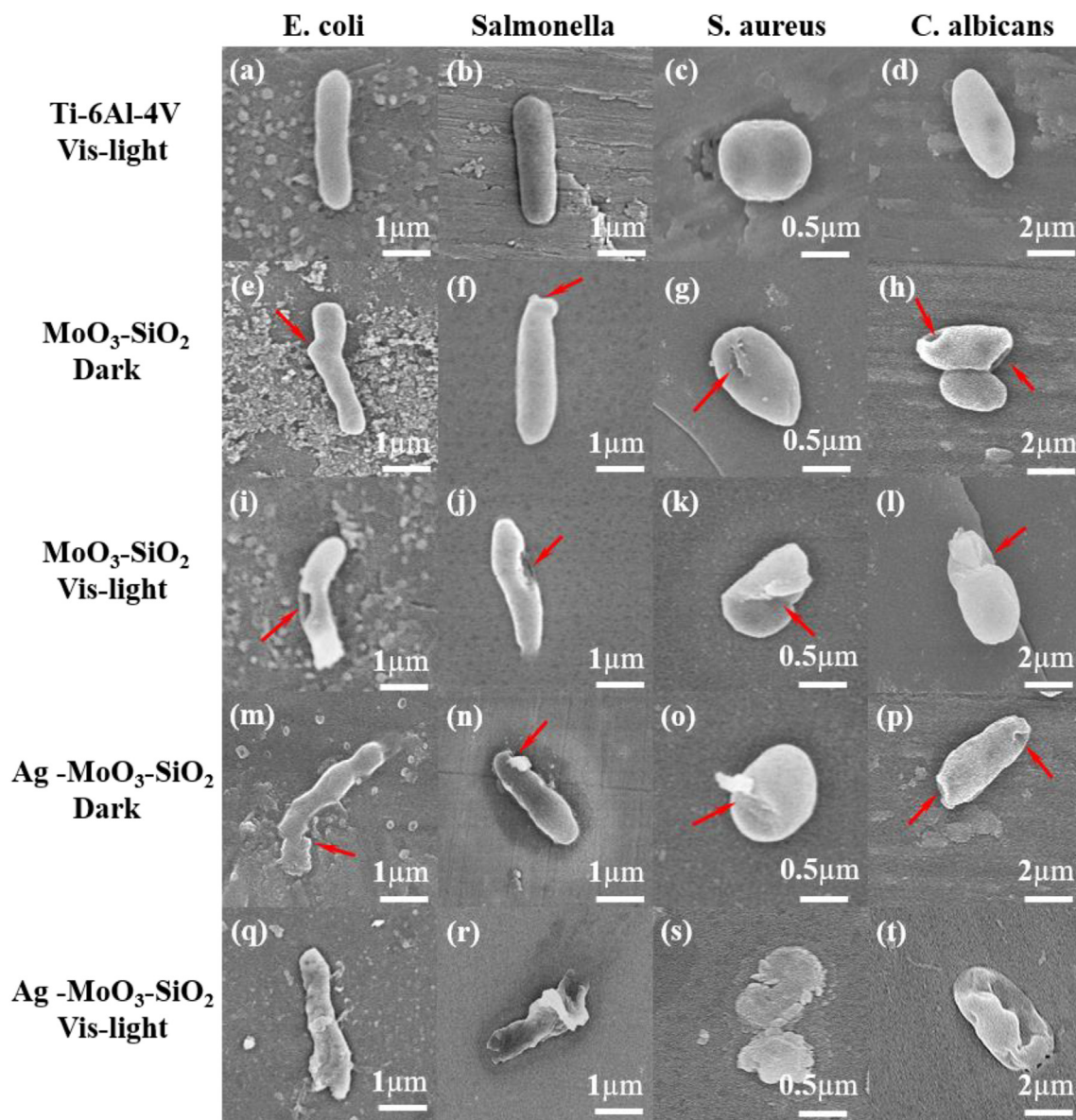
Fig. 12. FE-SEM images of four bacterial cells after 1 h exposed to Ti-6Al-4V, Ag-free MoO₃-SiO₂ and Ag-containing MoO₃-SiO₂ coatings.

mechanism is responsible for the biocidal activity or fungicidal activity of the Ag-free coating without light irradiation. For the Ag-containing coating, the presence of nanoscale Ag_2O phase is more soluble than metallic Ag and regarded as a source to provide sustained release of Ag^+ ions. The Ag^+ cations anchor on the cellular membrane, which is coordinated with H_3O^+ ions, altering the cell wall permeability and disturbing the normal respiratory of bacteria cells [59]. Ag^+ cations might seriously impede the replication of DNA molecules and inhibit a number of enzyme functions [61]. For example, as shown in Fig. 12(o), the detached fragments (marked with red arrowhead) adhere to the surface of the *S. aureus* bacteria cell, together with deep grooves on cell membrane, implying that synergistic action between Ag^+ and H_3O^+ ions produces more destructive than their individual effects. Under visible light irradiation condition, the additional photocatalytic in-activation mechanism of bacteria strains can be closely linked to oxidative damage induced by the resultant ROS, including hydrogen peroxide (H_2O_2) and hydroxyl radicals ($\cdot OH$), which have a lethal effect on bacteria cells [6]. The major mechanism behind the bactericidal activity endowed by the oxidative attack of ROS derives from two aspects: (1) the negatively charged hydroxyl radicals are firstly to destroy the outer membrane bacteria, inducing changes in permeability of reactive

species [14]; (2) the hydrogen peroxide can directly penetrate the cell membrane and arouse the structural and functional disordering of the inner membrane, eventually causing the cell death [3,6]. For instance, as shown in Fig. 12(k), after1 h irradiation, the surface of *S. aureus* bacteria cell cultured on the Ag-free coating appear wrinkled and ir-regular, clearly evidencing the severe morphological and structural injuries for cell membranes. At the same irradiation time, *S. aureus* bacteria cells cultured on the Ag-containing coating (Fig. 12(s)) exhibit completely lysed and collapsed, and large amounts of leakage of the cellular components cause cell death. These results indicate that Ag_2O-incorporated coating exhibit greater bactericidal ability than the Ag-free coating under photocatalytic condition, which is intimately asso-ciated with an enhanced photocatalytic activity by the introduction of Ag_2O. The MoO_3-SiO_2-Ag_2O coating exhibits high capability at killing microbes through multiple antimicrobial approaches to function si-multaneously, including bacterial shedding properties by surface hy-drophobic nature and synergistic action of the release of Ag^+ ions, surface acidic reaction and photocatalytic activity on inactivation of bacteria. Therefore, the coating may be a promising candidate for biomedical applications to protect of health-care devices from patho-gens transmission. Fig. 13 displays the schematic diagrams of potential
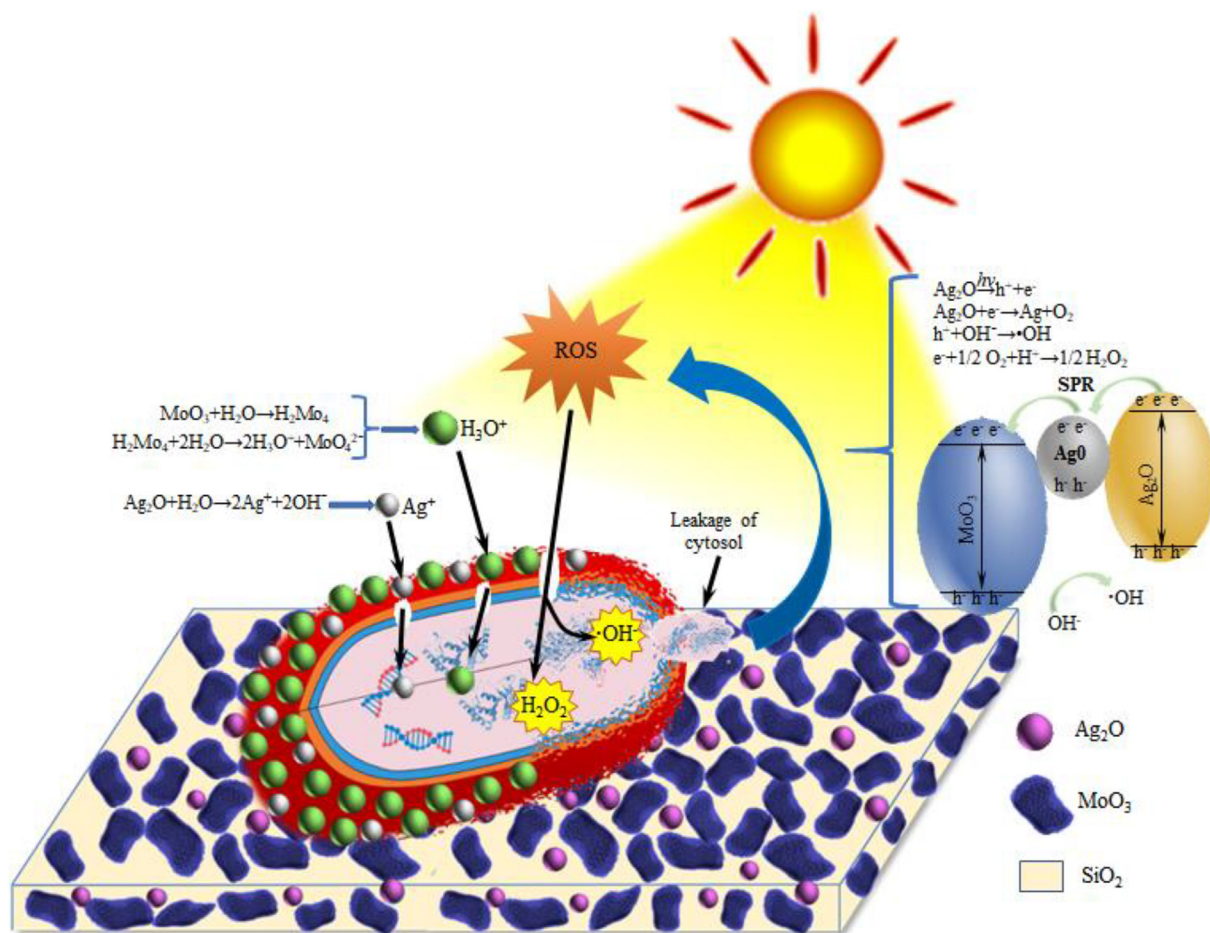
Fig. 13. Schematic diagram illustrating the potential bactericidal mechanism of Ag-containing MoO_3-SiO_2 nanocomposite coating.

antibacterial mechanisms for the MoO_3-SiO_2-Ag_2O coating.

5. Conclusions

In summary, a novel MoO_3-SiO_2-Ag_2O nanocomposite antibacterial coating was fabricated on a Ti–6Al–4V substrate by reactive sputter-deposition. The newly developed coating is composed of nano-crystal-lite MoO_3 and small amounts of Ag_2O dispersedly distributed in amorphous SiO_2 matrix. Moreover, the coating exhibits good hydro-phobicity property and adhesion strength between the coating and substrate. The RhB photodegradation tests suggest that the MoO_3-SiO_2-Ag_2O coating exhibits much greater photocatalytic activities than the MoO_3-SiO_2 coating, which was attributed to enhanced photodegrada-tion rate by the introduction of Ag_2O. Antibacterial activity tests under both dark and visible light conditions indicate that the MoO_3-SiO_2-Ag_2O coating has stronger bactericidal properties than the MoO_3-SiO_2 coating not only to Gram-negative and Gram-positive bacteria, but also to fungi. The desirable antimicrobial activity of this coating derives from the combined effects of surface hydrophobicity, the release of Ag^+ ions, surface acidic reaction and photocatalytic activity, which can be used to reduce hospital-acquired infections.

Declaration of competing interest

No any financial interests/personal relationships which may be considered as potential competing interests.

References

[1] C. Zollfrank, K. Gutbrod, P. Wechsler, J.P. Guggenbichler, Antimicrobial activity of transition metal acid MoO_3 prevents microbial growth on material surfaces, Mater. Sci. Eng. C Mater. Biol. Appl. 32 (1) (2012) 47–54.
[2] R. Rebelo, S.V. Calderon, R. Fangueiro, M. Henriques, S. Carvalho, Influence of oxygen content on the antibacterial effect of Ag-O coatings deposited by magnetron sputtering, Surf Coat Tech 305 (2016) 1–10.
[3] S. Shafaei, D. Van Opdenbosch, T. Fey, M. Koch, T. Kraus, J.P. Guggenbichler, C. Zollfrank, Enhancement of the antimicrobial properties of orthorhombic mo-lybdenum trioxide by thermal induced fracturing of the hydrates, Mater. Sci. Eng. C Mater. Biol. Appl. 58 (2016) 1064–1070.
[4] I.M. Gould, Costs of hospital-acquired methicillin-resistant Staphylococcus aureus (MRSA) and its control, Int. J. Antimicrob. Agents 28 (5) (2006) 379–384.
[5] S. Harbarth, S. Cosgrove, Y. Carme, Effects of antibiotics on nosocomial epide-miology of vancomycin-resistant enterococci, Antimicrob Agents Ch 46 (6) (2002) 1619–1628.
[6] J. Bogdan, J. Zarzynska, J. Plawinska-Czarnak, Comparison of infectious agents susceptibility to photocatalytic effects of nanosized titanium and zinc oxides: a practical approach, Nanoscale Res. Lett. 10 (1) (2015) 1023.
[7] T. Fu, Y.G. Shen, Z. Alajmi, S.Y. Yang, J.M. Sun, H.M. Zhang, Sol-gel preparation and properties of Ag-TiO2 films on surface roughened Ti-6Al-4V alloy, Mater. Sci. Technol. 31 (4) (2015) 501–505.
[8] C. Adlhart, J. Verran, N.F. Azevedo, H. Olmez, M.M. Keinanen-Toivola, I. Gouveia, L.F. Melo, F. Crijns, Surface modifications for antimicrobial effects in the healthcare setting: a critical overview, J Hosp Infect 99 (3) (2018) 239–249.
[9] S. Wu, X. Liu, A. Yeung, K.W. Yeung, R.Y. Kao, G. Wu, T. Hu, Z. Xu, P.K. Chu, Plasma-modified biomaterials for self-antimicrobial applications, ACS Appl. Mater. Interfaces 3 (8) (2011) 2851–2860.

[10] H. Liu, T. Lv, C. Zhu, Z. Zhu, Direct bandgap narrowing of TiO₂/MoO₃ heterostructure composites for enhanced solar-driven photocatalytic activity, Sol. Energy Mater. Sol. Cells 153 (2016) 1–8.

[11] B. Onat, V. Butun, S. Banerjee, I. Erel-Goktepe, Bacterial anti-adhesive and pH-induced antibacterial agent releasing ultra-thin films of zwitterionic copolymer micelles, Acta Biomater. 40 (2016) 293–309.

[12] N. Ekthammathat, A. Phuruangrat, T. Thongtem, S. Thongtem, Synthesis and characterization of Ce-doped CuO nanostructures and their photocatalytic activities, Mater. Lett. 167 (2016) 266–269.

[13] J. Wang, Y. Xia, Y. Dong, R.S. Chen, L. Xiang, S. Komarneni, Defect-rich ZnO nanosheets of high surface area as an efficient visible-light photocatalyst, Applied Catalysis B-Environmental 192 (2016) 8–16.

[14] J. Gamage McEvoy, Z. Zhang, Antimicrobial and photocatalytic disinfection mechanisms in silver-modified photocatalysts under dark and light conditions, J Photochem Photobiol C: Photochem Rev 19 (2014) 62–75.

[15] M. Pérez-González, M. Morales-Luna, J. Santoyo-Salazar, H. Crotte-Ledesma, P.E. García-Tinoco, S.A. Tomás, Improved adsorption and photocatalytic removal of methylene blue by MoO₃ thin films: role of the sputtering power, film thickness, and sputtering working pressure, Catal. Today (2020), https://doi.org/10.1016/j.cattod.2019.06.003 in press.

[16] N. Tetault, H. Gbaguidi-Haore, X. Bertrand, R. Quentin, N. van der Mee-Marquet, Biocidal activity of metalloacid-coated surfaces against multidrug-resistant microorganisms, Antimicrob Resist In 1 (1) (2012) 35.

[17] K. Krishnamoorthy, M. Veerapandian, K. Yun, S.J. Kim, New function of molybdenum trioxide nanoplates: toxicity towards pathogenic bacteria through membrane stress, Colloids Surf B Biointerfaces 112 (2013) 521–524.

[18] J. Xu, T.T. Sun, S. Jiang, P. Munroe, Z.-H. Xie, Antimicrobial and biocorrosion-resistant MoO₃-SiO₂ nanocomposite coating prepared by double cathode glow discharge technique, Appl. Surf. Sci. 447 (2018) 500–511.

[19] P. Pereira-Silva, A. Costa-Barbosa, D. Costa, M.S. Rodrigues, P. Carvalho, J. Borges, F. Vaz, P. Sampaio, Antifungal activity of ZnO thin films prepared by glancing angle deposition, Thin Solid Films 687 (2019) 137461.

[20] L.J. Wang, F. Zhang, A. Fong, K.M. Lai, P.W. Shum, Z.F. Zhou, T. Fu, P. Ning, S.Y. Yang, Tungsten film as a hard and compatible carrier for antibacterial agent of silver, J. Mater. Sci. 53 (15) (2018) 10640–10652.

[21] J. Xu, Z. Li, P. Munroe, Z.-H. Xie, Oxidation resistance of Mo(Si₁₋ₓAlₓ)₂ nanocrystalline films and characterization of their oxide scales by electrochemical impedance spectroscopy, RSC Adv. 4 (99) (2014) 55696–55708.

[22] D. Xiang, H. Xia, W. Yang, P. Mou, Parametric study and residual gas analysis of large-area silicon-nitride thin-film deposition by plasma-enhanced chemical vapor deposition, Vacuum 165 (2019) 172–178.

[23] C. Vasilescu, S.I. Drob, J.M.C. Moreno, P. Osiceanu, M. Popa, E. Vasilescu, M. Marcu, P. Drob, Long-term corrosion resistance of new Ti-Ta-Zr alloy in simulated physiological fluids by electrochemical and surface analysis methods, Corros. Sci. 93 (apr) (2015) 310–323.

[24] G. Greczynski, L. Hultman, X-ray photoelectron spectroscopy: towards reliable binding energy referencing, Prog. Mater. Sci. 107 (2020).

[25] C. Xiang, L. Sun, Y. Wang, G. Wang, X. Zhao, S. Zhang, Large-scale, uniform and superhydrophobic titania nanotubes at the inner surface of 1000-mm-long titanium tubes, J. Phys. Chem. C 121 (2017) 15448–15455.

[26] C. Xiang, L. Sun, General way to compute the intrinsic contact angle at tubes, J. Phys. Chem. C 122 (51) (2018) 29210–29219.

[27] M.L. Zhao, H.H. Gong, M. Ma, L. Dong, M.D. Huang, R.X. Wan, H.Q. Gu, Y.B. Kang, D.J. Li, A comparative antibacterial activity and cytocompatibility for different top layers of TiN, Ag or TiN-Ag on nanoscale TiN/Ag multilayers, Appl. Surf. Sci. 473 (2019) 334–342.

[28] B. Yan, Z. Zheng, J.X. Zhang, H. Gong, Z.X. Shen, W. Huang, T. Yu, Orientation controllable growth of MoO₃ nanoflakes: micro-Raman, field emission, and birefringence properties, J. Phys. Chem. C 113 (47) (2009) 20259–20263.

[29] X. Liu, W. Li, F. Wang, H. Li, C. Ren, Y. Zhao, A systematic study on polymerization and photocatalytic performance by investigating Ag₂O·x(MoO₃) (x = 1, 2, 3, 4) photocatalysts, Catalysis Science & Technology 8 (21) (2018) 5544–5556.

[30] B.M. Reddy, B. Chowdhury, P.G. Smirniotis, An XPS study of the dispersion of MoO₃ on TiO₂–ZrO₂, TiO₂–SiO₂, TiO₂–Al₂O₃, SiO₂–ZrO₂, and SiO₂–TiO₂–ZrO₂ mixed oxides, Appl. Catal. A Gen. 211 (1) (2001) 19–30.

[31] Y. Du, D. Tang, G. Zhang, X. Wu, Facile synthesis of Ag₂O-TiO₂/sepiolite composites with enhanced visible-light photocatalytic properties, Chin. J. Catal. 36 (12) (2015) 2219–2228.

[32] X. Jing, X. Peng, X. Sun, W. Zhou, W. Wang, S. Wang, Design and synthesis of Mo₂C/MoO₃ with enhanced visible-light photocatalytic performance for reduction of Cr (VI) and degradation of organic pollutants, Mater. Sci. Semicond. Process. 100 (2019) 262–269.

[33] B. Liu, L. Mu, B. Han, J. Zhang, H. Shi, Fabrication of TiO₂/Ag₂O heterostructure with enhanced photocatalytic and antibacterial activities under visible light irradiation, Appl. Surf. Sci. 396 (2017) 1596–1603.

[34] H. Sinaim, D.J. Ham, J.S. Lee, A. Phuruangrat, S. Thongtem, T. Thongtem, Free-polymer controlling morphology of α-MoO₃ nanobelts by a facile hydrothermal synthesis, their electrochemistry for hydrogen evolution reactions and optical properties, J. Alloys Compd. 516 (2012) 172–178.

[35] Y. Wang, L. Zhu, M. Wang, N. Ren, A facile of route of synthesizing Fe doped

[36] amorphous SiO₂ film-containing crystal TiO₂ on carbon steel by PEO, Int. J. Hydrog. Energy 41 (35) (2016) 15710–15716.

[36] Q.M. Ahkam, E.U. Khan, J. Iqbal, A. Murtaza, M.T. Khan, Synthesis and characterization of cobalt-doped SiO₂ nanoparticles, Phys. B Condens. Matter 572 (2019) 161–167.

[37] M. Khairy, M.M. Mohamed, S.M. Reda, A. Ibrahem, Effect of annealing temperature and Ag contents on the catalytic activity and supercapacitor performances of Ag@Ag₂O/RGO nanocomposites, Mater. Sci. Eng. B 242 (2019) 90–103.

[38] D. Valencia, L. Díaz, L.F. Ramírez-Verduzco, M.A. Amezcua-Allieri, J. Aburto, MoO₃-based catalysts supported on SiO₂ and their performance in hydro-deoxygenation, Mater. Lett. 251 (2019) 226–229.

[39] J.V. Silveira, J.A. Batista, G.D. Saraiva, J. Mendes Filho, A.G. Souza Filho, S. Hu, X. Wang, Temperature dependent behavior of single walled MoO₃ nanotubes: a Raman spectroscopy study, Vib. Spectrosc. 54 (2) (2010) 179–183.

[40] F. Chandoul, A. Boukhachem, F. Hosni, H. Moussa, M.S. Fayache, M. Amlouk, R. Schneider, Change of the properties of nanostructured MoO₃ thin films using gamma-ray irradiation, Ceram. Int. 44 (11) (2018) 12483–12490.

[41] K.D. Parghi, R.V. Jayaram, Sequential oxidation and condensation of alcohols to benzimidazoles/benzodiazepines by MoO₃–SiO₂ as a heterogeneous bifunctional catalyst, Catal. Commun. 11 (15) (2010) 1205–1210.

[42] J. Hu, H. Xu, S. Wang, W. Jia, Y. Cao, In-situ solid-state synthesis and regulation of Ag₂O/Ag₂CO₃ heterojunctions with promoted visible-light driven photocatalytic decomposition for organic pollutant, Sep. Purif. Technol. 226 (2019) 95–108.

[43] M. Dieterle, G. Weinberg, G. Mestl, Raman spectroscopy of molybdenum oxides, Phys. Chem. Chem. Phys. 4 (5) (2002) 812–821.

[44] S. Phadungdhitidhada, P. Mangkorntong, S. Choopun, N. Mangkorntong, Raman scattering and electrical conductivity of nitrogen implanted MoO₃ whiskers, Ceram. Int. 34 (4) (2008) 1121–1125.

[45] M.S. Kabir, P. Munroe, Z. Zhou, Z. Xie, Scratch adhesion and tribological behaviour of graded Cr/CrN/CrTiN coatings synthesized by closed-field unbalanced magnetron sputtering, Wear 380–381 (2017) 163–175.

[46] M.S. Kabir, P. Munroe, V. Gonçales, Z. Zhou, Z. Xie, Structure and properties of hydrophobic CeO₂₋ₓ coatings synthesized by reactive magnetron sputtering for biomedical applications, Surf. Coat. Technol. 349 (2018) 667–676.

[47] S. Wang, Y. Zhang, T. Chen, G. Wang, Preparation and catalytic property of MoO₃/SiO₂ for disproportionation of methyl phenyl carbonate to diphenyl carbonate, J. Mol. Catal. A Chem. 398 (2015) 248–254.

[48] K. Saravanakumar, M.M. Ramjan, P. Suresh, V. Muthuraj, Fabrication of highly efficient visible light driven Ag/CeO₂ photocatalyst for degradation of organic pollutants, J. Alloys Compd. 664 (2016) 149–160.

[49] A. Singh, S. Kumar, B. Ahmed, R.K. Singh, A.K. Ojha, Temperature induced modifications in shapes and crystal phases of MoO₃ for enhanced photocatalytic degradation of dye waste water pollutants under UV irradiation, J. Alloys Compd. 806 (2019) 1368–1376.

[50] Q. Zhang, F. Han, Y. Yan, Q. Dai, G. Proctor, P. Cheah, P. Avijit, R.P. Chandra, N. Kang, M. Hu, B. Yao, Preparation and properties of visible light responsive RGO/In₂TiO₅ nanobelts for photocatalytic degradation of organic pollutants, Appl. Surf. Sci. 485 (2019) 547–553.

[51] M. Yang, Y. Pu, W. Wang, J. Li, X. Guo, R. Shi, Y. Shi, Highly efficient Ag₂O/AgNbO₃ p-n heterojunction photocatalysts with enhanced visible-light responsive activity, J. Alloys Compd. 811 (2019).

[52] A. Phuruangrat, S. Siri, P. Wadbua, S. Thongtem, T. Thongtem, Microwave-assisted synthesis, photocatalysis and antibacterial activity of Ag nanoparticles supported on ZnO flowers, J. Phys. Chem. Solids 126 (2019) 170–177.

[53] B. Zheng, Z. Wang, X. Wang, Y. Chen, Enhanced photocatalytic properties of defect-rich alpha-MoO₃ nanoflakes by cavitation and pitting effect, J. Hazard. Mater. 378 (2019) 120753.

[54] W. Zhou, H. Liu, J. Wang, D. Liu, G. Du, J. Cui, Ag₂O/TiO₂ nanobelts heterostructure with enhanced ultraviolet and visible photocatalytic activity, ACS Appl. Mater. Interfaces 2 (8) (2010) 2385–2392.

[55] K. Lorenz, S. Bauer, K. Gutbrod, J.P. Guggenbichler, P. Schmuki, C. Zollfrank, Anodic TiO₂ nanotube layers electrochemically filled with MoO₃ and their antimicrobial properties, Biointerphases 6 (1) (2011) 16–21.

[56] Y. Li, J. Zhao, G. Zhang, L. Zhang, S. Ding, E. Shang, X. Xia, Visible-light-driven photocatalytic disinfection mechanism of Pb-BiFeO₃/rGO photocatalyst, Water Res. 161 (2019) 251–261.

[57] A. Gao, R. Hang, X. Huang, L. Zhao, X. Zhang, L. Wang, B. Tang, S. Ma, P.K. Chu, The effects of titania nanotubes with embedded silver oxide nanoparticles on bacteria and osteoblasts, Biomaterials 35 (13) (2014) 4223–4235.

[58] P. Ganguly, C. Byrne, A. Breen, S.C. Pillai, Antimicrobial activity of photocatalysts: fundamentals, mechanisms, kinetics and recent advances, Appl. Catal. B Environ. 225 (2018) 51–75.

[59] S. Ciuca, M. Badea, E. Pozna, I. Pana, A. Kiss, L. Floroian, A. Semenescu, C.M. Cotrut, M. Moga, A. Vladescu, Evaluation of Ag containing hydroxyapatite coatings to the Candida albicans infection, J. Microbiol. Methods 125 (2016) 12–18.

[60] Y. Jin, Z. Dai, F. Liu, H. Kim, M. Tong, Y. Hou, Bactericidal mechanisms of Ag₂O/TNBs under both dark and light conditions, Water Res. 47 (5) (2013) 1837–1847.

[61] V.H. Matsubara, F. Igai, R. Tamaki, P. Tortamano Neto, A.E. Nakamae, M. Mori, Use of silver nanoparticles reduces internal contamination of external hexagon implants by Candida albicans, Braz. Dent. J. 26 (5) (2015) 458–462.